Sub-surface processes and heat fluxes at coarse-blocky Murtèl rock glacier (Engadine, eastern Swiss Alps)

Dominik Amschwand[1], Jonas Wicky[1], Martin Scherler[1,†], Martin Hoelzle[1], Bernhard Krummenacher[2], Anna Haberkorn[2], Christian Kienholz[2], and Hansueli Gubler[3]

[1]Department of Geosciences, University of Fribourg, Fribourg, Switzerland
[2]GEOTEST AG, Zollikofen/Bern, Switzerland
[3]Alpug GmbH, Davos, Switzerland
[†]deceased, 4 June 2022

Abstract. We estimate the sub-surface energy budget and heat fluxes in the coarse-blocky active layer (AL) of the Murtèl rock glacier, a seasonally snow-covered permafrost landform located in the eastern Swiss Alps. In the highly permeable AL, conductive/diffusive heat transfer including thermal radiation, non-conductive heat transfer by air circulation (convection), and heat storage changes from seasonal accretion and melting of ground ice shape the ground thermal regime. We quantify indi-
5 vidual heat fluxes based on a novel in-situ sensor array in the AL and direct observations of the ground ice melt in the years 2020–2022. Two thaw-season mechanisms render Murtèl rock glacier comparatively climate-resilient. First, the AL intercepts $\sim 70\%$ ($55-85\,\mathrm{MJ\,m^{-2}}$) of the thaw-season ground heat flux by melting ground ice that runs off as meltwater, $\sim 20\%$ ($10-20\,\mathrm{MJ\,m^{-2}}$) is spent on heating the blocks, and only $\sim 10\%$ ($7-13\,\mathrm{MJ\,m^{-2}}$) is transferred into the permafrost body beneath and causes slow permafrost degradation. Second, the effective thermal conductivity in the ventilated AL increases
10 from $1.2\,\mathrm{W\,m^{-1}\,K^{-1}}$ under strongly stable temperature gradients to episodically over $10\,\mathrm{W\,m^{-1}\,K^{-1}}$ under unstable temperature gradients, favouring convective cooling by buoyancy-driven Rayleigh ventilation (thermal semiconductor effect). In winter, radiatively cooled air infiltrating through a discontinuous, semi-closed snowcover leads to strong AL cooling. The two characteristic parameters (effective thermal conductivity and intrinsic permeability) are sensitive to debris texture, hence these convective undercooling processes are specific to highly permeable coarse-blocky material.

15 ## 1 Introduction

The cooling effect of a coarse-blocky active layer (AL) is well known from field studies and arises from an interplay of several heat transfer and storage mechanisms in a permeable buffer layer between ground and atmosphere or seasonal snow cover (Johansen, 1975; Wakonigg, 1996). Heat transfer processes in a permeable coarse-blocky AL are convective/advective heat transport by moving moist air/water, conduction within the blocks, and long-wave radiation in the pore space between the
20 blocks. Additionally, heat is stored or released by sensible temperature changes of the rock mass and by phase changes of water, ice and vapour, including refreezing/melt of ice in the active layer and evaporation/sublimation. Snow with its high surface albedo, low thermal conductivity, and latent heat sink upon melting crucially shapes the ground thermal regime (Mellor, 1977; Zhang, 2005; Luetschg et al., 2008). For a concise overview of the heat exchange processes specific to 'cold rocky landforms'

(Brighenti et al., 2021) like rock glaciers or scree slopes, we refer to Haeberli et al. (2006); Millar et al. (2014). The relative
25   contribution of each flux to the total flux across the permeable, multiphase coarse-blocky AL depends on the topography,
properties like texture and particle size distribution (e.g., intrinsic permeability that determines importance of convection), and
time-varying meteorological conditions (e.g., air density stratification in the AL or snow cover that control buoyancy-driven
air convection) (Johansen, 1975; Herz, 2006). These controlling parameters vary laterally and vertically (e.g., porosity and
permeability decrease towards the AL base (Mollaret et al., 2020; Wicky and Hauck, 2020)) and also change over time, and so
30   do the dominant heat transfer mechanisms.

   The effect of undercooling has been known for a long time from field investigations (Bächler, 1930; Wakonigg, 1996;
Harris and Pedersen, 1998; Kneisel et al., 2000; Gorbunov et al., 2004; Delaloye and Lambiel, 2005; Sawada et al., 2003;
Delaloye and Lambiel, 2005; Herz, 2006; Millar et al., 2014; Popescu et al., 2017b), but exact processes have remained
elusive. These knowledge gaps were also addressed on Murtèl rock glacier in the Engadine (eastern Swiss Alps), a hot spot of
35   mountain permafrost research (Hoelzle et al., 2002), with a series of studies. Large seasonal deviations of the estimated surface
energy balance (SEB) were attributed to unmeasured and insufficiently represented non-conductive sub-surface heat transfer
processes in the AL (Hoelzle et al., 1999, 2001; Mittaz et al., 2000). First field studies dedicated to the sub-surface (AL)
heat transfer processes have been published by Hanson and Hoelzle (2004, 2005) based on their temperature measurements
in the uppermost $90 \, \text{cm}$ of the AL and previous, then-unpublished works (Oswald, 2004; Naguel, 1998). Important insights
40   about the near-surface AL heat transfer processes and interaction with the snow cover have been gained, but the quantitative
understanding was insufficient to reliably estimate heat fluxes. Next, the thermal characterization of the coarse-blocky material
with geophysical methods (electrical resistivity tomography, refraction seismics tomography) has been an important next step
towards AL heat transfer modelling (Schneider et al., 2012, 2013), that has been carried out by Scherler et al. (2014). Air
circulation and convective heat transfer, long suspected to be the primary heat transfer mechanism to shape the thermal regime
45   in highly permeable coarse-blocky debris, have been investigated in the field by (Oswald, 2004; Panz, 2008; Schneider, 2014)
and studied numerically by Wicky and Hauck (2017, 2020). In parallel, another important field study on the micro-climate of
coarse-blocky scree has been carried out by Herz et al. (2003a, b); Herz (2006) in the Matter Valley (western Swiss Alps).
They have described the heat transfer processes in detail and estimated thermal diffusivities and heat fluxes, but for the lack
of appropriate measurements could not verify them. One of the few comprehensive data sets beyond ground temperatures in
50   mountain permafrost has been gathered by Rist and Phillips (2005); Rist (2007). They deployed a heat flux plate, ultrasound
probes, conductometer, vapour traps and reflectometer probes to characterise the ground hydro-thermal regime of a steep,
permafrost-underlain scree slope. To summarize, several heat transfer processes have been successfully simulated separately,
for example buoyancy-driven air circulation (Wicky and Hauck, 2017, 2020), purely conductive processes from the interplay
between a low-conductive ground and snow cover (Gruber and Hoelzle, 2008), or the interplay between sensible and latent
55   heat storage (Renette et al., 2023). However, few microclimatological studies attempted to simultaneously parametrize all heat
fluxes (Mittaz et al., 2000; Hoelzle et al., 2001; Stocker-Mittaz et al., 2002; Hoelzle et al., 2003; Hoelzle and Gruber, 2008;
Scherler et al., 2014), and few comprehensive sub-surface hydro-thermal measurements beyond ground temperatures exist in
blocky mountain permafrost (Rist et al., 2003; Rist and Phillips, 2005). Also, AL properties like the thermal conductivity are

poorly investigated for such coarse blocky material as on Murtèl, where individual blocks have volumes of $\sim 0.1 \, \mathrm{m}^3$ (up to $1-10 \, \mathrm{m}^3$). Lacking better knowledge, empirical engineering relations developed for sand or gravel were often extrapolated to such large blocks. Without in-situ data, it is unclear whether such extrapolations are valid.

In this work, a follow-up study on Amschwand et al. (2023) where the surface energy balance (SEB) was estimated, we carry the investigations on rock glacier Murtèl further and return to the field with a novel in-situ sensor array installed in natural cavities of the AL pore space. The sub-surface measurements go beyond the previous ground temperature recordings and include relative humidity, airflow speed, long-wave radiation, and direct heat flux measurements. The aim is to quantitatively describe conductive, radiative and convective sub-surface fluxes, estimate the thaw-season AL heat budget, and characterize the ground thermal properties. We address three questions: (1) Where does the heat go to during the thaw season (ground heat fluxes and AL energy budget)? (2) How is the heat transferred in the AL (heat transfer and storage mechanisms)? (3) What is the effective thermal conductivity of the AL?

We estimate the heat fluxes with two approaches and compare the results to examine their consistency and to deal with the uncertainties. First, heat fluxes are measured directly by two pyrgeometer and two heat flux plates (HFPs). They are however prone to measurement errors and inevitably variable, because the HFPs are much smaller than a representative elementary volume (REV), the scale where a volume average describes the AL in an apparently homogeneous material (averaging over the constituents rock, air, and water) and where so-called *effective* parameter (like the effective thermal conductivity k_{eff}) are applicable (e.g., Roth and Boike, 2001). The REV length scale is at least that of characteristic block or pore size (Nield and Bejan, 2017), i.e. in such coarse blocky material roughly $\geq 0.1-1 \, \mathrm{m}$. Hence, the very local heat flux plate measurements might not be as representative of the average vertical AL fluxes as the pyrgeometer measurements that hemispherically integrate over the inner cavity surface ('REV uncertainty'). Second, we estimate the heat fluxes with the calorimetric method from AL temperature changes (sensible heat storage changes) and ground-ice melt observations (latent heat storage changes). We present to our knowledge the first seasonal ground-ice observations in a rock-glacier coarse-blocky AL. Based on the observed rate of change of the ground-ice table depth, we sketch a modified Stefan scheme and a turbulent degree-day-model to simulate seasonal ground-ice ablation (*calorimetric method*). These flux estimations provide an AL energy budget for the thaw season.

This work contributes to the quantitative process understanding of heat transfer in the active layer of a ventilated coarse-blocky permafrost landform. The flux measurements and inferred ground thermal properties are valuable to calibrate or validate numerical models of the ground thermal regime and the ice–water balance. The simple parameterisations of the thaw-season heat fluxes are a step towards the quantification of ground-ice melt in mountain permafrost and, since ground ice melt in ice-rich permafrost landforms is energy-limited, towards the hydrological role of rock glaciers.

2 Study site

The studied Murtèl rock glacier (WGS 84: 46°25′47″N, 9°49′15″E; CH1903+/LV95: 2'783'080, 1'144'820; 2620–2700 m asl.; Fig. 1) is located in a north-facing periglacial area of Piz Corvatsch in the Upper Engadine, a slightly continental, rain-shadowed high valley in the eastern Swiss Alps. Mean annual air temperature (MAAT) is $-1.7°\mathrm{C}$, mean annual precipitation is
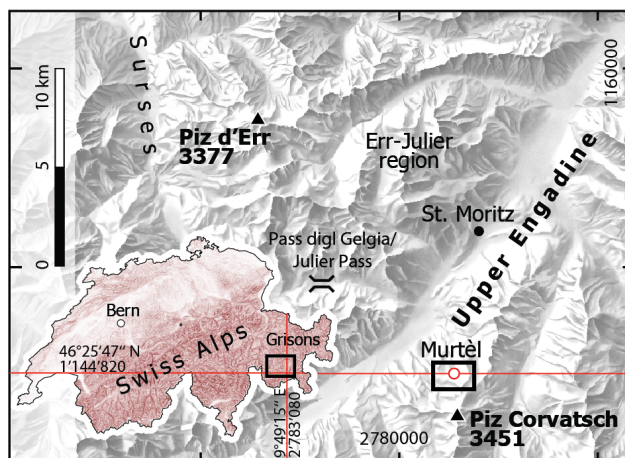
Figure 1. Location of Murtèl rock glacier in the Upper Engadine, a high valley in the eastern Swiss Alps. Inset map: Location and extent (black rectangle) of regional map within Switzerland (source: Swiss Federal Office of Topography swisstopo).

~ 900 mm (Scherler et al., 2014). The tongue-shaped, single-unit (monomorphic sensu Frauenfelder and Kääb (2000)), active rock glacier is surrounded by steep rock faces and is in direct connection with a talus slope (2700–2850 m asl.), ~ 250 m long, and ~ 150 m wide. Crescent-shaped furrows ($\sim 3-5$ m deep) and ridges with steep, in places near-vertical slopes dissect the overall gently northnorthwestward dipping surface ($\sim 10-12°$, $< 15°$, Guodong et al. (2007)) and create a pronounced furrow-and-ridge microtopography in the lowermost part of the rock glacier (Kääb et al., 1998). The snow cover is thicker and lasts longer in furrows than on ridges, influencing the ground thermal regime on a small scale (Bernhard et al., 1998; Keller and Gubler, 1993; Hoelzle et al., 2003). In the colder furrows, the otherwise 3–5 m thick, coarse-grained and clast-supported debris mantle is only ~ 2 thick. The ground ice table is accessible in a few places.

The stratigraphy to a depth of 60 m is known from several boreholes (Vonder Mühll and Haeberli, 1990; Vonder Mühll, 1996; Arenson et al., 2002, 2010). The coarse-blocky AL is 3 m thick on average (2–5 m) and consists of large blocks typically with 0.1 to 2 m edge length (Scherler et al., 2014). A few boulders reach dimensions of $\sim 3-5$ m. Fine material ($\leq$sand) is sparse near the surface, but its volume fraction varies laterally and increases with depth (inverse grading (Haeberli et al., 2006)). The AL has a poor water retention capacity. Supra-permafrost water drains within hours–days at the AL base (Tenthorey and Gerber, 1991) and is not considered to significantly modify the ground thermal properties. The vast, connected pores create a high intrinsic permeability (Wicky and Hauck, 2020). Beneath the coarse-blocky debris mantle, roughly coinciding with the thermally defined AL, lies the perennially frozen ice-supersaturated rock glacier core. Drill cores have revealed sand- and silt-bearing massive ice (3–28 m depth, ice content over 90% vol.), although boreholes drilled within ~ 30 m distance suggest some lateral small-scale heterogeneity (Vonder Mühll and Haeberli, 1990; Arenson et al., 2010).

3 Measurements and data processing

3.1 Field observations and instrumentation

We use measurements from the PERMA-XT sensor cluster presented in (Amschwand et al., 2023), where the above-surface sensors are described. Most of the below-surface sensors were installed in one natural cavity of the coarse-blocky AL that was large enough for a human to enter and deep enough to come close to the AL base (Figs. 2, 3). A narrow passage covered by a large block ('lid') leads into a spacious 'main chamber' with its 'floor' at $2\,\text{m}$ depth. A narrow extension reaches a depth of $3\,\text{m}$. Its base is covered by wet fine material (gravel, sand). The cavity in the clast-supported coarse-blocky AL is enclosed by large blocks with voids in between, allowing air circulation. In August 2020, this comparatively large cavity (dimensions $\sim 2 \times 1.5 \times 3\,\text{m}$) was instrumented with sensors to measure the temperature, humidity, long-wave radiation, heat flux and AL airflow speed at several depths down to $3\,\text{m}$. Detailed sensor specifications of the sub-surface sensors are given in Table 1, and the locations are shown in Fig. 3 and Table 2. One thermistor string is suspended in air (TK1), another one (TK6) has its five thermistors drilled $5\,\text{cm}$ into the blocks at depths corresponding to the TK1 thermistors. Relative humidity is measured at two levels, 0.7 (HV5/1) and $2.0\,\text{m}$ (HV5/2) beneath the surface. Three thermo-anemometer record wind speed at three levels, close to the surface (WS/3 at $-0.35\,\text{m}$), mid-cavity (WS/2 at $-1.5\,\text{m}$), and in a narrow extension at depth (WS/1 at $-2.1\,\text{m}$). Two TriSonica Mini ('TR3') mounted perpendicular to each other measured the three-dimensional wind field at mid-cavity level, next to the WS/2. A back-to-back pair of pyrgeometer mounted at mid-cavity level (CGR3 at $-1.55\,\text{m}$) measures the upward and downward long-wave radiation in the cavity. Two heat flux plates are cemented onto the rock surface, one at the underside of a near-surface block (HFP/2 at $-1.1\,\text{m}$), another one on the cavity 'floor' (HFP/1 at $-2.0\,\text{m}$). Since accurate distances are required for the calculation of vertical gradients and fluxes, we triangulated the relative height of the sensors in the instrumented cavity with a Leica DISTO X310 laser distance and goniometer. The instrumented main cavity was completely destroyed by rockfall on 20 September 2023.

Additional thermistor strings and thermo-anemometer were installed in the vicinity at different micro-topographical location to reveal the spatial pattern of temperature and airflow. One additional thermo-anemometer in a similar cavity $20\,\text{m}$ away (WS/4), together with another air-suspended thermistor string (TK5), one near the surface beneath a wind-swept large block on a ridge (WS/5, 'wind hole'), and one near the surface in a nearby rock glacier furrow (WS/6). The sub-surface sensor array is completed by 10 autonomous miniature temperature loggers (UTL; Table 1) distributed on the rock glacier to grasp the variability of the near-surface ground temperature.

The ground ice is accessible at a few spots, all located in furrows where the AL is thinner ($1-2\,\text{m}$). In one spot, a plastic tube was drilled ca. $120\,\text{cm}$ into the ice in August 2009 (C. Hilbich, pers. comm.). We made serendipitous use of it as an 'ablation stake', manually measuring the height of the ground-ice table at each field visit in summer 2022. One UTL3 (UTL #2735) is placed there $\sim 0.5\,\text{m}$ beneath terrain surface.

Additionally, we use borehole temperature data provided by the Swiss Permafrost Monitoring Network (PERMOS) for basal conductive heat flux from the rock glacier core and point-wise surface radiation data from the PERMOS automatic weather station (Noetzli et al., 2019).
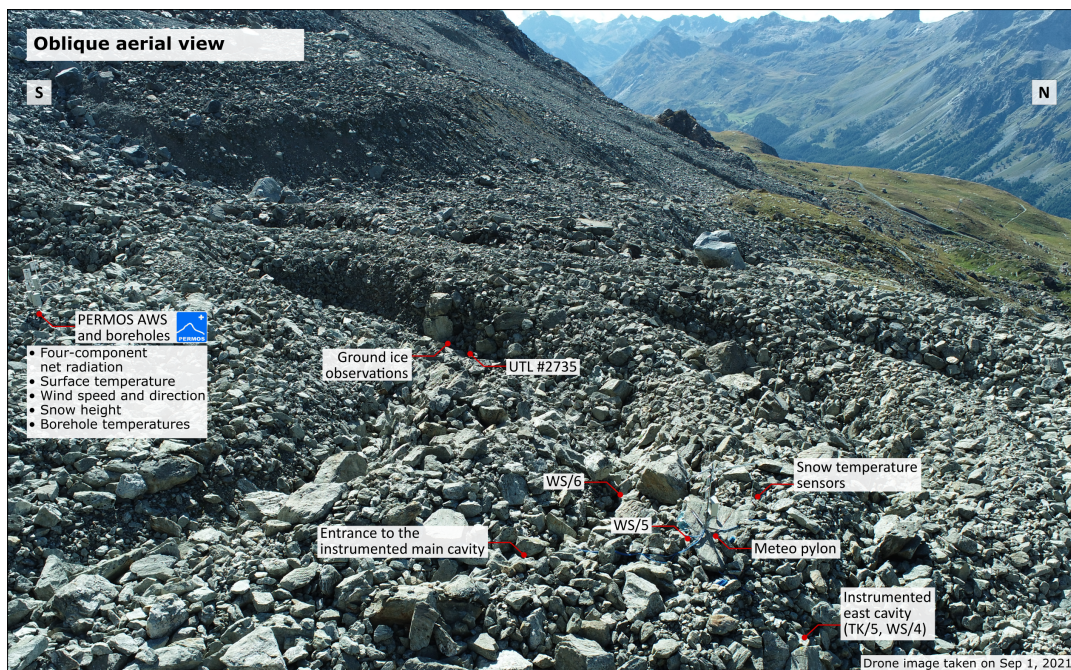
Figure 2. Oblique aerial view of the Murtèl rock glacier (foreground) and location of the above-surface sensors and the ground-ice observations in the rock glacier furrow.

Table 1. PERMA-XT sub-surface sensor specifications.

Quantity [unit]	Manufacturer	Sensor type	Accuracy
AL air temperature $T_{al}(z)$ [°C]	TE Connectivity[a]	44031RC NTC thermistor chain TK1/1–5	± 0.1°C
AL relative humidity $q_a(z)$ [%]	CSI[b]	HygroVUE5 hygrometer	± 0.3°C; $\leq \pm 4\%$
Rock temperature $T_r(z)$ [°C]	TE Connectivity[a]	44031RC NTC thermistor chain TK6/1–5 (drilled 5 cm into the blocks)	± 0.1°C
Long-wave radiation L_{al} [W m^{-2}]	Kipp & Zonen	CGR3 pyrgeometer (4.5−42 µm, FoV 150°)	< 2 W m^{-2}
Heat flux [W m^{-2}]	Hukseflux	HFP01 heat flux plate	site-specific
Airflow speed proxy[c] [-]	Hukseflux	TP01 thermal properties sensor (formerly WS01) (artificial leaf used as hot-film anemometer[e])	$\leq \pm 25\%$ or $\leq \pm 0.2$ m s^{-1}
Airflow velocity (u,v,w) [m s^{-1}]	Anemoment/LI-COR	TriSonica Mini ultrasonic anemometer	± 0.2 m s^{-1} ± 1°
Near-surface ground temperature [°C]	GEOTEST	UTL3 miniature temperature logger with YSI 44005 NTC thermistors	± 0.1°C $(T \leq \pm 20$°C)

Measurement range and accuracy by manufacturer/vendor. The specifications of the PERMOS sensor are given in Scherler et al. (2014) and Hoelzle et al. (2022).
[a] Thermistor strings manufactured by Waljag GmbH. [b]CSI: Campbell Scientific, Inc. [c]Airflow speed derived from the measured heat flux.
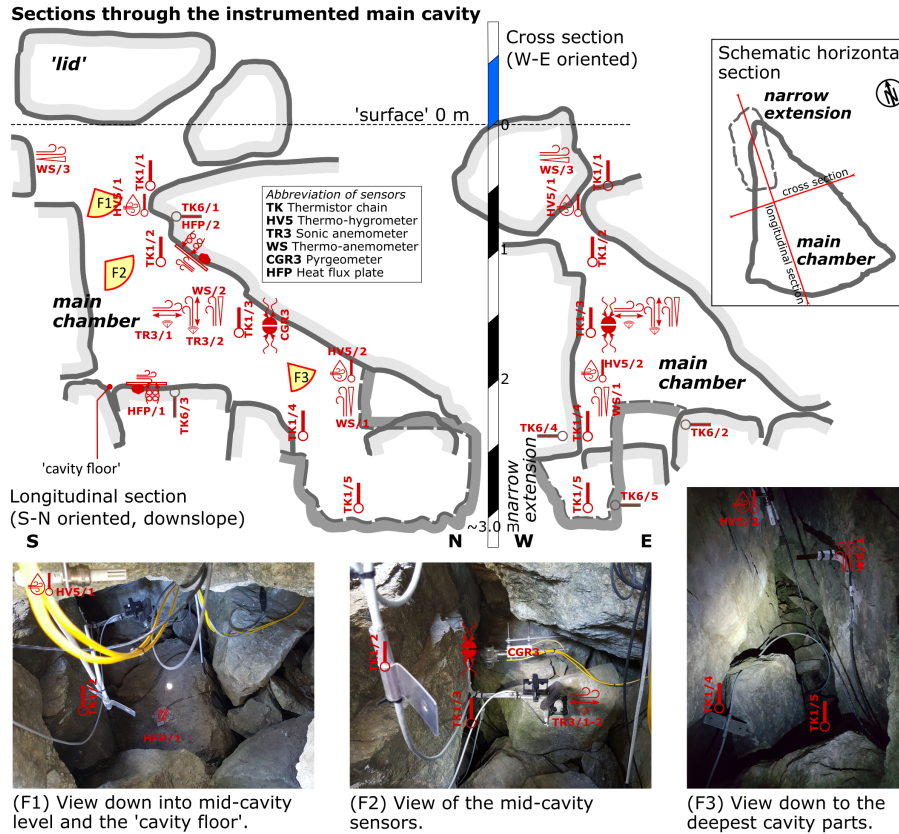
Figure 3. Schematic sections and images of the instrumented main cavity with locations of the sensors.

3.2 Data processing

145 We analyse the data of two years from Sep 1, 2020, to Sep 30, 2022. The above-surface sensors and the corresponding data processing (air temperature, relative humidity, precipitation, snow height) are described in Amschwand et al. (2023).

3.2.1 Sub-surface long-wave radiation

The net radiative flux in the AL Q^{rad}_{CGR3} is calculated from the long-wave radiation of a back-to-back pyrgeometer pair installed in the instrumented cavity (as in Amschwand et al. (2023)),

150 $$Q^{rad}_{\mathrm{CGR3}} = (L^{\downarrow}_{al} - L^{\uparrow}_{al}) \tag{1}$$

as the difference between the upwards $L^{\uparrow}_{al}$ and downwards $L^{\downarrow}_{al}$ long-wave radiation components.

7

Table 2. PERMA-XT subsurface sensor locations and approximate depth beneath the surface.

Sensor name	Location	Sensor name	Location
TK1/1–5	AL air temperature profile TK1/1: -0.5 m TK1/2: -1.1 m TK1/3: -1.6 m TK1/4: -2.4 m TK1/5: -2.9 m	TK6/1–5	AL rock temperature profile TK6/1: -0.7 m TK6/2: -1.8 m TK6/3: -2.1 m TK6/4: -2.4 m TK6/5: -2.9 m
HV5/1–2	AL relative humidity and temperature HV5/1: -0.7 m; HV5/2: -2.0 m		
CGR3	Long-wave radiation in main cavity (Q_{CGR3}^{rad}) -1.55 m, upward and downward-facing	HFP/1–2	Heat flux plate in main cavity HFP/2: -1.1 m on underside of near-surface block HFP/1: -2.0 m on 'cavity floor' (Q_{HFP})
WS/1–6	Wind-speed proxy WS/3: -0.35 m; WS/2: -1.5 m; WS/1: -2.1 m WS/4: in 'east cavity' -0.3 m WS/5: 'wind hole' at the surface WS/6: in rock glacier furrow -0.3 m	TR3	sonic wind speeds -1.5 m
UTL #2735	near-surface air temperature near the 'ablation stake' -0.5 m		

The abbreviations correspond to Fig. 3.

The raw outputs $L_{raw}^{\uparrow/\downarrow}$ of the two pyrgeometers in the instrumented cavity are corrected by accounting for the long-wave radiation emitted by the instruments themselves (Kipp & Zonen CGR3 manual, 2014) as in Amschwand et al. (2023)

$$L_{al}^{\uparrow/\downarrow} = L_{raw}^{\uparrow/\downarrow} + \sigma T_{\mathrm{CGR3}}^4, \qquad (2)$$

155   with the pyrgeometer housing temperature T_{CGR3}. Large ($> 0.5°$C) or rapid changes of the housing temperature differences between the back-to-back mounted pyrgeometer hint at dust or water deposition on the upward-facing pyrgeometer window. Such disturbed measurements showed up in the high-resolution (10 minutes) data, but did not significantly affect the daily net long-wave radiation balance in the sheltered cavity.

3.2.2 Sub-surface airflow speed

160   We refer to the sub-surface 'wind' in the cavity as 'airflow' to differentiate it from the atmospheric wind. We deployed two sensor types to measure the airflow speed in the AL, five distributed thermo-anemometer (Hukseflux TP01, Table 1) and a sonic anemometer in the instrumented cavity (TriSonica Mini 'TR3', Table 1).

Thermo-anemometer

Measurements of an airflow speed proxy in the AL pore space were performed with six Hukseflux TP01 (formerly WS01; Table 1) sensor consisting of a heated foil that measures a cooling rate, expressed as a heat transfer coefficient h_{WS} [W m^{-2} K^{-1}]. h_{WS} is related to airflow speed via $u_{\mathrm{WS}} = (h_{\mathrm{WS}} - 5)/4$. This empirical linearised relation is valid with reasonable accuracy for airflow speeds in the range of $0.1 - 2$ m s^{-1} (Hukseflux WS01 manual, 2006). The TP01 sensor does not resolve the direction of the airflow (hence the term 'speed' instead of 'velocity'). One measurement cycle takes 1 min and consists of three measurements to detect any offset, one initial measurement before heating, one at 30 s, and a final one after cool-down at 60 s. The deviation of the linearized relation to the common engineering relation Nu $:= hL/k_a = 0.6\,\mathrm{Re}^{0.5}$ (Schuepp, 1993) is within 0.2 m s^{-1} for $u_{\mathrm{WS}} < 0.6$ m s^{-1}. Hence, the measurements are qualitative rather than absolute. Although the foils were oriented parallel to the dominant airflow direction that can be expected from the local cavity geometry, any airflow perpendicular to the foil creates turbulence that affects the heat transfer efficiency. At very low wind speeds or if the sensor is much warmer than the surrounding air (a large Richardson number), buoyancy effects become important relative to forced convection and disturb the airflow speed measurement (increases h_{WS}). Also, deposition and evaporation of liquid water can disturb the measurements (increases h_{WS}), as was revealed by wrapping the heated foils in moist tissues. WS measurements during precipitation events at shallow levels, where water may infiltrate, are discarded. Repeated zero-point checks were performed throughout the snow-free season by enclosing the heated foil in small and dry plastic bags for a few hours, ensuring stagnant conditions with zero airflow speed. Neither a drift nor a temperature dependency beyond the measurement uncertainty was detected.

Ultrasonic anemometer

Two TriSonica Mini anemometer (herein abbreviated as 'TR3'; Table 1) mounted perpendicular to each other at 1.5 m depth logged the three airflow velocity components at a resolution of 10 Hz and sent 10-second averages (TriSonica Mini sensor manual, 2021). The post-processing consisted of spike removals (outlier), drift correction (Butterworth high-pass filter with a cut-off frequency of $(5\,\mathrm{days})^{-1}$), and zero checks.

3.2.3 Heat flux plates

The heat flux plate (HFP) itself adds another resistance to the heat flow from the rock slab interior to the cavity ('resistance error'; Hukseflux HFP manual (2016)) which is within 20% and sufficient in our context, given the field conditions and the REV uncertainty. The heat flux plates are cemented onto the block surface to avoid air gaps and to minimise the contact resistance. We assess the resistance error by conceptualizing the heat flow through the block and the HFP into the open cavity as a series (thermal resistance network). The total resistance R_{tot} is the sum of the conductive resistance in the rock slab within a 'zone of influence' of the HFP given by the sensor diameter d_{HFP}, $R_r = d_{\mathrm{HFP}}/k_r \approx 80 \times 10^{-3}$ m$/2.5$ W m^{-1} K^{-1}, the HFP resistance $R_{\mathrm{HFP}} = 71 \times 10^{-4}$ K m^2 W^{-1}, and the interfacial radiative-convective resistance R_s between the rock surface and the cavity, i.e. $R_{tot} = R_r + R_{\mathrm{HFP}} + R_s$. An upper bound for R_s is the stagnant (no convection), radiation-only

inverse heat transfer coefficient $1/h_{rad} = (4\varepsilon\sigma\bar{T}^3)^{-1} \approx 1/5 \text{ K m}^2 \text{ W}^{-1}$ ($\varepsilon \approx 1$). Hence, the HFP is the least resistive link of
the heat transfer chain.

4 Parameterisations and heat flux modelling

4.1 Energy budget of the Murtèl coarse-blocky active layer (AL)

The ground heat flux Q_G [W m^{-2}] from the ground surface downwards into the coarse-blocky AL is spent on warming the
debris ΔH_{al}^θ (sensible heat storage changes), melting ground ice in the AL Q_m (latent heat storage changes), and conducted
into the permafrost body beneath Q_{PF} ('permafrost heat flux') (cf. Hayashi et al., 2007; Woo and Xia, 1996),

$$Q_G - (\Delta H_{al}^\theta + Q_m + Q_{\text{PF}}) = 0 \text{ [W m}^{-2}]. \tag{3}$$

The fluxes are counted as positive if they provide energy to the reference volume, the AL. We use different approaches to
independently estimate each term in Eq. 3 (Sect. 4.3) and compare with direct measurements (Sects. 3.2.1, 3.2.3).

4.2 Heat transfer and air circulation

Heat is transferred by three basic modes — *convection/advection* by moving fluid parcels (air/water), the emission/absorption
of electromagnetic *radiation*, and thermal *conduction* by molecular interaction — whose dominance in unfrozen (excluding
latent heat effects) porous materials such as soils under field conditions is controlled by equivalent particle size and degree of
water saturation (Johansen, 1975). These heat transfer modes combined result in the ground heat flux Q_G (Eq. 3). In coarse
debris far from water saturation, the most important heat transfer modes are *air convection*, heat carried by air circulation, and
long-wave radiation (Q_r), radiative heat transfer between blocks of different temperatures by electromagnetic waves that travel
across the pore space (Fillion et al., 2011). Heat advection by intercepted rainfall that percolates to the ground-ice table results
in a small rain heat flux Q_{Pr} (part of Q_G in Eq. 3). *Heat conduction* alone compared to radiation is considered negligible in the
coarse-blocky AL because the contact areas between the blocks are too small in the clast-supported debris (cf. Esence et al.,
2017), but transfers the heat within the blocks and also in the permafrost body beneath the AL, Q_{PF} (Scherler et al., 2014;
Schneider, 2014). Hence, we conceptualise conductive heat transfer within the blocks and radiative heat transfer between the
blocks as a heat transfer chain in series, and denote it as conductive–radiative.

Furthermore, it is useful to differentiate two types/modes of air convection according to the driving force, (i) buoyancy-
driven and (ii) forced convection (Nield and Bejan, 2017). *Buoyancy-driven convection* refers to air set in motion by air density
instabilities within the coarse-blocky AL, i.e. when denser ($\sim$colder, drier) air is on top of lighter ($\sim$warmer, more moist) air,
and is driven by gravity. The entire unstable air column is set in motion. It has a cooling effect: Comparatively colder air sinks
into the coarse-blocky AL, displaces the warmer air, and subsequently impedes the penetration of warmer air. Warmer air is
evacuated rapidly (*Balch effect*). The vigour of buoyancy-driven convection in a porous medium is a function of the Rayleigh–
Darcy number Ra defined as (Nield and Bejan, 2017; Johansen, 1975; Kane et al., 2001; Herz, 2006; Côté et al., 2011; Wicky

and Hauck, 2020)

$$\text{Ra} := \frac{\rho_a C_p}{k_{\text{eff}}^0} \frac{g \beta_a K h_{al} \Delta T_a}{(\mu_a / \rho_a)}, \tag{4}$$

where ρ_a is the air density [kg m^{-3}], C_p the isobaric specific heat capacity [J kg^{-1} K^{-1}], k_{eff}^0 the stagnant (absence of convection) bulk thermal conductivity of the AL [W m^{-1} K^{-1}], $\beta_a \approx 1/T_0$ the thermal expansion coefficient [(273 K)$^{-1}$], K the intrinsic AL permeability estimated with the Kozeny–Carman equation [2×10^{-5} m^2, Eq. 20] (Herz, 2006; Côté et al., 2011; Wicky and Hauck, 2020), h_{al} the AL layer thickness [m], ΔT the temperature difference across the AL [K or °C], μ_a the air dynamic viscosity [Pa s], and g the gravitational acceleration [9.81 m s^{-2}]. Buoyancy-driven convection can be expected when Ra exceeds a threshold value (critical Rayleigh number Ra$_c$), commonly given as 27 in open voids or 40 beneath a snow cover.

Wind-forced convection or *continuous air exchange with the atmosphere* (Humlum, 1997; Harris and Pedersen, 1998; Kane et al., 2001; Juliussen and Humlum, 2008) refers to air set in motion by external wind, i.e. at the ground surface. Wind gusts propagating into the permeable AL (shear flow, momentum diffusion by rough surface) lead to forced mechanical mixing. It can rapidly cool or warm the ground, depending on the air temperature relative to the ground temperature. The mixing is most pronounced near the surface and decays with depth (Evatt et al., 2015).

4.3 Flux estimations

The fluxes and storage changes/conversions (terms in Eq. 3) are estimated as follows, going from the surface to the permafrost body. The rain heat flux is estimated from the rain gauge data (Sect. 4.3.1). AL fluxes are estimated with the calorimetric method based on AL temperature measurements (sensible heat storage changes, Sect. 4.3.2) and ground-ice melt observations (melt energy, Sect. 4.3.3). The heat flux at the AL base is estimated with the gradient method (Sect. 4.3.4).

4.3.1 Rain heat flux Q_{Pr}

The flux of infiltrating rainwater r [m^3 m^{-2} s^{-1}] is the intercepted rainwater that rapidly percolates to the ground ice table and is cooled from the initial precipitation temperature T_P to 0°C (at the most) (Sakai et al., 2004; Hayashi et al., 2007). It releases the following sensible heat flux

$$Q_{Pr} = C_w r (T_P - 0°C), \quad \text{if } h_S = 0, \, T_{wb} \geq 2°C. \tag{5}$$

with the volumetric heat capacity $C_w = \rho_w c_w$ [10^3 kg m$^{-3} \times 4.2$ kJ kg^{-1} K^{-1}], and snow height h_S [m]. As a conservative estimate, the rainwater is assumed to be cooled from surface temperature $T_P := T_s$ to the freezing point. Precipitation data is taken from the on-site rain gauge, assuming that precipitation is liquid based on a threshold air temperature of $T_{wb} = 2°C$ (Amschwand et al., 2023). Water contributions from upslope flowing onto the rock glacier and liquid precipitation falling into the snowpack is not accounted for (no precipitation measurements available as long as the rain gauge is snow covered).

4.3.2 Sensible heat storage changes ΔH_{al}^θ

The sensible heat ΔH_{al}^θ stored/released by temperature changes of the blocks are estimated as in Amschwand et al. (2023) by

$$255 \quad \Delta H_{al}^\theta = \int_{-h_{al}}^{0} \frac{\mathrm{d}}{\mathrm{d}t}\{(1-\phi_{al})\rho_r c_r T_r(z)\}\,\mathrm{d}z \approx (1-\phi_{al})\frac{\langle\rho_r c_r\rangle}{\Delta t_r}\sum_i\{\langle\bar{T}_a(z_i,t+\Delta t_r)\rangle - \langle\bar{T}_a(z_i,t)\rangle\}\Delta z_i \qquad (6)$$

with $h_{al} = 3$ m the AL thickness, ρ_r the rock density [2690 kg m^{-3}] (Corvatsch granodiorite, Schneider (2014)), c_r the specific heat capacity [790 J kg^{-1} K^{-1}], AL porosity $\phi_{al} = 0.4$ (Scherler et al., 2014), and $T_r(z)$ and $T_a(z)$ the vertical rock and in-cavity air temperature profile [°C], respectively. In the discretised formulation, the temperatures $\langle\bar{T}(z_i)\rangle$ are layer-wise averages in the i-th layer with thickness Δz_i (denoted by $\langle\cdot\rangle$), derived from the thermistor string TK1/1 and the radiometric
260 surface temperature T_s. Since AL water contents are always low enough not to significantly influence the heat capacity, $C_v = (1-\phi_{al})\rho_r c_r$ is a time-invariant, fixed AL thermal property (Scherler et al., 2014).

4.3.3 Melt energy Q_m

The latent heat Q_m consumed by melting ground ice is estimated from the 'ablation measurements' via

$$Q_m = f_i L_m \rho_i \frac{\mathrm{d}\zeta}{\mathrm{d}t}, \qquad (7)$$

265 where ζ is the observed depth of the ground-ice table [m]. f_i [−], L_m [3.34×10^5 J kg^{-1}], and ρ_i [kg m^{-3}] are the volumetric ice content, latent heat of melting, and ice density, respectively.

4.3.4 AL base flux through permafrost body Q_{PF}

The heat flux across the permafrost table Q_{PF} is estimated with the gradient method from PERMOS borehole temperature data via Fourier's heat conduction equation

$$270 \quad Q_{\text{PF}} = -k_{\text{PF}}\frac{\mathrm{d}T}{\mathrm{d}z} \approx -k_{\text{PF}}\frac{\Delta T_{\text{PF}}}{\Delta z}, \qquad (8)$$

where the borehole temperatures are measured at 4 and 5 m depth in the permafrost body beneath the AL. We take a thermal conductivity k_{PF} value of 2.5 W m^{-1} K^{-1} (Vonder Mühll and Haeberli, 1990; Scherler et al., 2014).

4.4 Parameterisations of the ground-ice melt

We test two approaches to parameterize the observed ground ice melt, (i) a temperature index model (degree-day model) applied
275 in simplified glacier models and also adopted to simulate sub-debris melt rates on debris-covered glaciers (e.g., Kayastha et al., 2000; Mihalcea et al., 2006), and (ii) the Stefan scheme commonly used in the permafrost research community to model ground thawing (e.g., Hayashi et al., 2007).

4.4.1 Temperature index model

A temperature index model (or 'degree-day model') is based on an empirical-statistical relationship between (most commonly)
280 air temperatures (differences) and melt rates (Hock, 2003),

$$
\frac{\Delta\zeta}{\Delta t} = \begin{cases} \hat{f}_m(T - T_0), & \text{if } T > T_0 \\ 0, & \text{if } T \leq T_0 \end{cases} \tag{9}
$$

with the empirical, site-specific melt factor f_m [cm day^{-1} $^\circ$C^{-1}] and an appropriately defined temperature difference $(T - T_0)$
[K, $^\circ$C]. Since this statistical relation is not process-based, appropriate temperatures are air, surface, or any ground temperature.
The value of $\hat{f}_m$ is determined by calibration.

285 ### 4.4.2 Stefan parameterisation

If the ground heat flux is mostly spent on melting ground ice the AL (assessed in Sect. 6.1.1), the rate of lowering the thaw
front/ground-ice table $d\zeta/dt$ [m s^{-1}] can be approximated with a linearised heat conduction equation (Hayashi et al., 2007),

$$
\rho_i f_i L_m \frac{d\zeta}{dt} = k_{\text{eff}} \frac{T_s - 0^\circ\text{C}}{\zeta}, \tag{10}
$$

whose solution is the Stefan equation of the form

290 $$
\zeta(t) = \sqrt{(2k_{\text{eff}} I(t))/(\rho_i f_i L_m)}, \tag{11}
$$

where k_{eff} is the effective thermal conductivity of the (unfrozen) AL above the thaw front/ground-ice table [W m^{-1} K^{-1}]
located at depth ζ [m] beneath ground surface (Fig. 4), and $I(t)$ the surface thaw index [$^\circ$C $\times$ s] (defined below). We emphasize
that the parameter k_{eff} plays a similar role to that of f_m in the index model, but with an important distinction: the value of k_{eff} is
set a priori from the AL thermal properties (outlined in Sect. 4.5) and not calibrated with the ablation data. Two modifications
295 are necessary to account for the AL stratigraphy on Murtèl (Fig. 4). First, the seasonal lowering of the ground ice table (assumed
to coincide with the thaw front) is modelled with a modified Stefan equation for a two-layered AL (Nixon and McRoberts,
1973; Kurylyk, 2015). In Eq. 11, the frozen ground is initially (at the onset of thaw season) uniform. However, on Murtèl, the
ice does not fill the AL pore space up to the ground surface. Rather, a layer (with thickness h_1) on top of the ice-saturated
AL remains nearly ice free year-round. This ice-poor overburden dampens ground-ice melt rates/thaw rates from the onset of
300 the thaw season. Apart from the different ground-ice content, the two layers share the same properties (porosity). The second
modification is a correction factor λ_5 for sensible heat storage changes in the thawed AL. λ_5 is derived from the Stefan number
Ste, $\lambda_5 = 1 - 0.16\,\text{Ste} + 0.038\,\text{Ste}^2$ (Kurylyk and Hayashi, 2016). The depth-averaged dimensionless Stefan number Ste defined
is proportional to the ratio of sensible heat to latent heat absorbed during thawing (Kurylyk and Hayashi, 2016),

$$
\text{Ste} := \frac{C_v \bar{T}_s}{L_m \langle f \rangle \rho_i}, \tag{12}
$$

305 with the bulk volumetric heat capacity $C_v = (1 - \phi_{al})\rho_r c_r$ [J m^{-3} $^\circ$C^{-1}] of the (unfrozen, ice-free) AL (identical for both
layers), the average surface temperature $\bar{T}_s$ for the time t elapsed since onset of the thaw season, and the latent heat consumed

by the melting of the ground ice $L_m \langle f \rangle \rho_i$ (different in each layer and depth-averaged denoted by $\langle \cdot \rangle$; details in Kurylyk and Hayashi (2016)).

With these two modifications, the equation for the thaw depth ζ [m] ('modified Berggren equation') from Kurylyk (2015);

310 Aldrich and Paynter (1953) simplifies to

$$
\zeta(t) = \begin{cases}
\sqrt{\frac{2k_{\mathrm{eff}} I_t(t)}{L_m f_1 \rho_i}}, & \text{if } I_t \leq I_1 \\
\sqrt{h_1^2 \left(1 - \frac{f_1}{f_2}\right) + \frac{2k_{\mathrm{eff}} I_t(t)}{L_m f_2 \rho_i}}, & \text{if } I_t > I_1
\end{cases}
\tag{13}
$$

with the effective thermal conductivity k_{eff} [W m^{-1} K^{-1}] of the (thawed/unfrozen) AL above the thaw front/ground-ice table, the volumetric pore ice content f of each layer (maximum at saturation, $f \leq \phi_{al}$), the pore ice density ρ_i [900 kg m^{-3}], and $I_t(t)$ the total surface thaw index [$^\circ$C $\times$ s], defined by

315
$$
I_t(t) := \int_0^t \lambda_5^2 T_s(t') \, \mathrm{d}t'.
\tag{14}
$$

In discretised form with daily average surface temperatures, $I_t(t_i) = 86400 \sum_i (\bar{\lambda}_5^2 \bar{T}_s)[t_i]$, summed over the i-th day since onset of the thaw season (Hayashi et al., 2007). Eq. 13 is premised on the assumption of (i) initial uniform temperature at the freezing point throughout the AL and uniform temperature beneath the thaw front (zero heat flux from the permafrost body beneath; Sect. 6.1.1), (ii) layer-wise homogeneous and time-invariant thermal properties and ground ice content, and

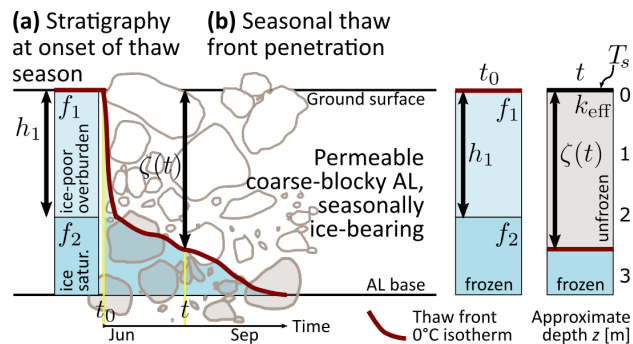320 (iii) quasi-steady state conditions (Kurylyk and Hayashi, 2016).

Figure 4. Ground-ice thaw and the Stefan equation. **(a)** Initial stratigraphy at the onset of the thaw season with ice-poor overburden and ice-saturated layer. **(b)** Seasonal thaw front penetration.

4.5 Estimation of AL thermal properties

We derive thermal properties of the AL, the effective thermal conductivity k_{eff} and the apparent thermal diffusivity κ_a, from in-situ measurements using two different approaches. k_{eff} and κ_a are related via the volumetric heat capacity C_v (Vonder Mühll

and Haeberli, 1990),

$$325 \quad \kappa_a = \frac{k_{\text{eff}}}{C_v} = \frac{k_{\text{eff}}}{(1 - \phi_{al})\rho_r c_r}. \tag{15}$$

Values for the porosity ϕ_{al}, rock density ρ_r, and the heat capacity c_r given in Sect. 4.3.2 yield $C_v = 1.275 \text{ MJ m}^{-3}$.

4.5.1 Effective thermal conductivity k_{eff} estimation

The effective thermal conductivity k_{eff} [W m^{-1} K^{-1}] is derived from the measured AL long-wave radiation Q_{CGR3}^{rad} (Eq. 1) and AL temperature gradients dT_{al}/dz using a diffusive flux-gradient relation of the form

$$330 \quad Q_{\text{CGR3}}^{rad} = -k_{\text{eff}} \frac{dT_{al}}{dz}. \tag{16}$$

It might seem odd to use Eq. 16, a diffusion equation formally identical to Fourier's heat conduction equation (cf. Eq. 8), since heat conduction is considered insignificant in the coarse-blocky AL (Sect. 4.2; discussed in Sect. 6.2.2). However, radiative heat transfer in a porous medium with opaque particles (rock) and transparent fluid (air) can be expressed as diffusive (Fillion et al., 2011; Lebeau and Konrad, 2016). The thermal conductivity k_{eff} is then rather a radiative conductivity than a purely
335 conductive one, denoted as an effective parameter.

4.5.2 Apparent thermal diffusivity κ_a estimation

The apparent thermal diffusivity κ_a [m^2 s^{-1}] is derived from measured AL temperatures T_{al} using the derivative method based on the one-dimensional transient thermal diffusion equation (Biot–Fourier equation) (Hinkel et al., 1990; Conway and Rasmussen, 2000),

$$340 \quad \frac{dT_{al}}{dt} = \kappa_a \frac{d^2 T_{al}}{dz^2}, \tag{17}$$

where T_{al} is the AL temperature [°C], t [s] is the time, and z is the AL depth [m]. The diffusivity as defined in Eq. 17 is an apparent parameter that lumps together conductive/radiative and non-conductive (convective) heat transfer in the coarse, highly permeable blocky material (Herz, 2006). We use only thaw season values where $T_{al} > 0.5°\text{C}$ to minimise effects of latent heat exchange. Day-to-day temperature change dT_{al}/dt and the second derivative $d^2 T_{al}/dz^2$ are calculated using the
345 Petersen et al. (2022) algorithm from daily average AL temperature data (TK1/2–4). To avoid spurious κ_a values, no κ_a is calculated for near-isothermal conditions (unstable numerics; Hinkel et al., 1990).

5 Measurement results

5.1 Ground thermal and moisture regime

The weather in each season differed markedly in the two years 2020–2022, which is reflected by the AL temperatures (Fig. 5).
350 Winter 2020–2021 was more snow-rich and lasted longer than the unusually snow-poor, short winter 2021–2022 with snow

disappearance in May–June, one month earlier than the usual melt-out in July. AL temperatures fluctuated more and attained lower values ($T_{al} < -8°\mathrm{C}$) in winter 2021–2022. Summer 2021 was comparatively cool-wet compared to the hot-dry summer 2022, with frequent passage of synoptic fronts bringing cold air and mixed precipitation (sleet). A few snow patches survived in the Murtèl catchment, which has rarely been occurring in the last ~ 15 years. In contrast, the summer 2022 was marked

355   by heat waves (in June, July) co-occurring with dry spells ($T_{al} > 10°\mathrm{C}$). The surface meteorological conditions are described further in Amschwand et al. (2023).
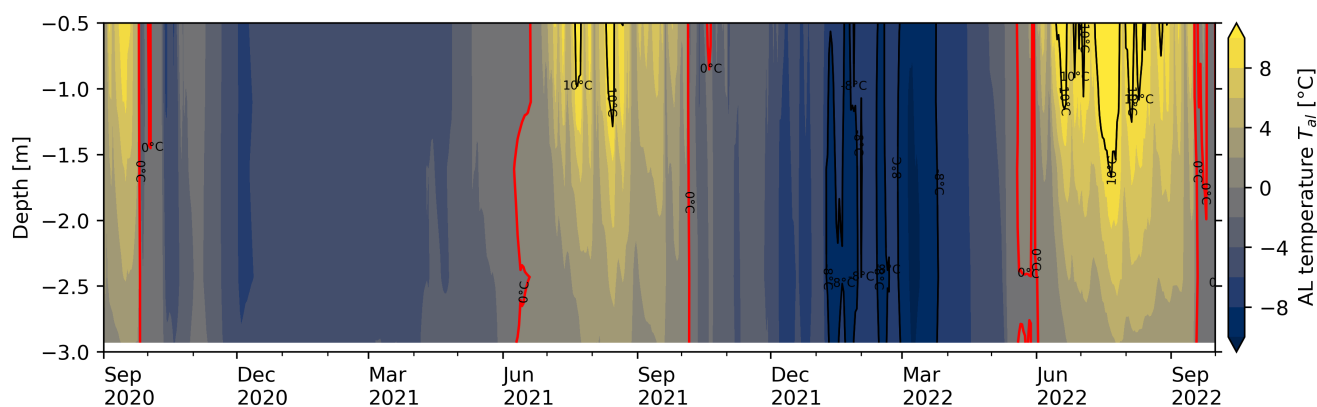
Figure 5. AL temperatures T_{al} in the instrumented main cavity (contour plot from TK1 data).

The Rayleigh-Darcy numbers show the stability of the AL air column (Fig. 6a; in the entire AL 0.5–2.4 m and a shallow sublayer 0.5–1.1 m). Ground temperature evolution is shown in Fig. 7. Autumn 2020 starts at the end of Sept with rapid cooling at high, supercritical Rayleigh numbers. Cooling continues more slowly throughout November, until a thick, 'closed'

360   snow cover stalled winter cooling in Dec 2020, when the snow height exceeded a threshold (60 cm as measured on a rock glacier ridge). The AL remained near-isothermal and near-isohume at sub-critical Ra numbers until May 2022. Summer 2022 was characterized by frequent shallow instabilities, i.e. super-critical Ra numbers in the uppermost 1 m of the AL. The deep AL remained stably stratified. The instabilities became more frequent and encompassed the entire AL in Oct 2021. In the snow poor winter 2021–2022, the snow cover remained 'open' as the snow height only rarely exceeded the threshold. AL

365   temperature kept fluctuating at occasionally sub-critical Ra numbers. In summer 2022, instabilities occurred not as frequent as in summer 2021.

The temperature profiles are specific to certain conditions that we mark with circled numbers ①–④ and use throughout this text. An overview is given in Table 3. The thaw season temperature profiles (Fig. 6b, ①) are near-linear down to daily timescale, but not on sub-diurnal timescales or on days with rapid cooling (Rayleigh ventilation ④, e.g., during the passage

370   of cold fronts). Thaw-season average temperature gradients are 2.0 K m^{-1} for 2021 ($R^2 = 0.995$) and 2.8 K m^{-1} for 2022 ($R^2 = 0.998$). The near-surface AL is often warmer and hence unstable with respect to the atmosphere despite the locally stable air stratification (nonlocal static stability sensu Stull (1991)). The winter averages (Dec–Mar) are near-isothermal in
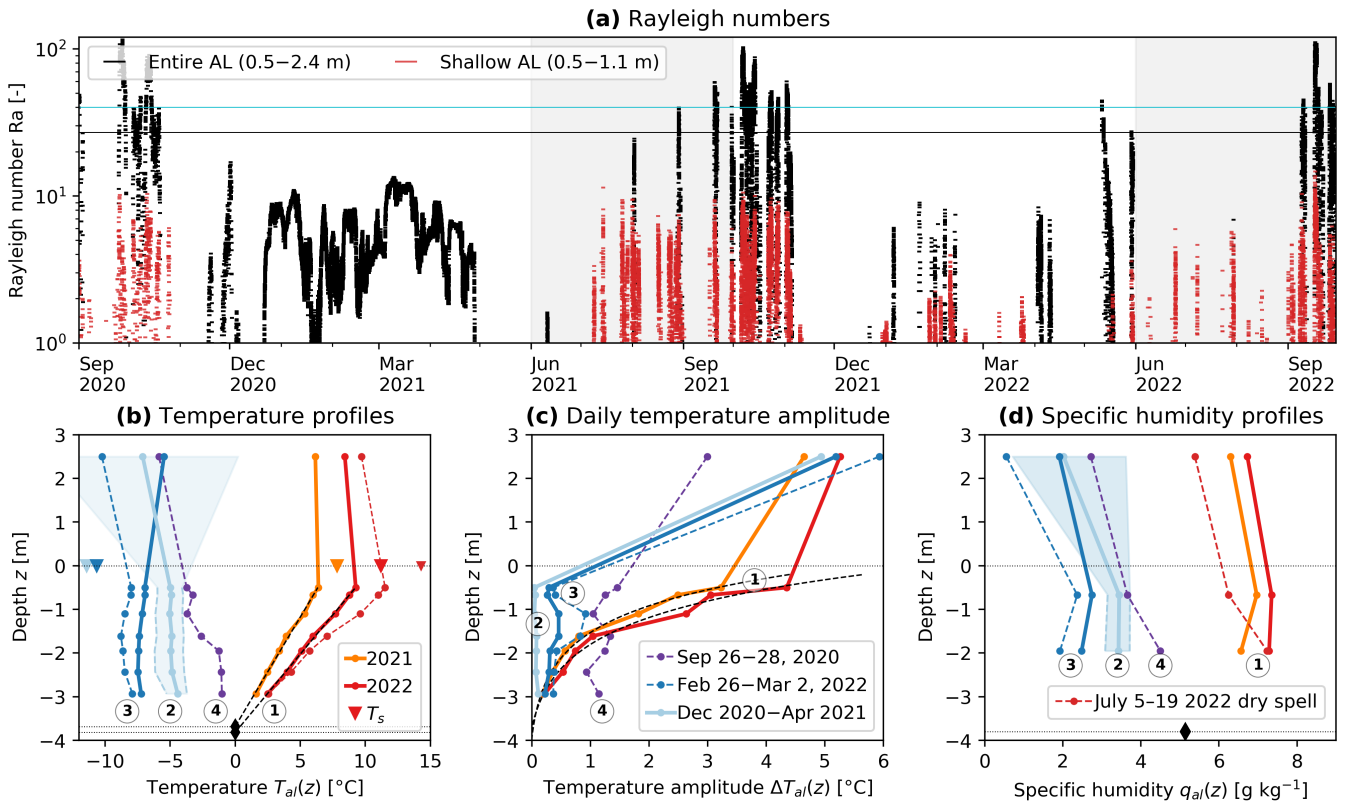
Figure 6. Ground thermal and moisture regime. **(a)**: Rayleigh numbers Ra indicate the air column stability (Eq. 4, 10 minute resolution). Onset of buoyancy-driven convection is potentially at $\mathrm{Ra} \geq \mathrm{Ra}_c$ of 27 in snowfree (black horizontal line) and 40 (cyan line) in snow-covered conditions. **(b)** Vertical temperature profiles ('trumpet curves') during selected periods (the circled numbers ①–④ refer to Table 3): ① summer/thaw season; ② stagnant winter conditions (Dec 2020–Apr 2021); ③ winter-time cold-air infiltration (winter average Dec 2021–Apr 2022, infiltration period Feb 26–March 2); ④ convective overturning by Rayleigh ventilation (event of Sep 26–28, 2020). **(c)** Amplitude of daily temperature variation (max–min). On a timescale of one day or longer, the thaw-season temperature profiles are near-linear and daily amplitude decays exponentially with depth, even in the comparatively large instrumented cavity. **(d)** Vertical specific humidity profiles.

winter 2020–2021 (②). In winter 2021–2022, occasional temperature minima at roughly $2\,\mathrm{m}$ depth ('bulges') hint at lateral cold air flow (Sect. 6.3, ③). The locally (near-)stable AL air is nonlocally unstable compared to the radiatively cooled snow surface with average surface temperature T_s of $-10°\mathrm{C}$ (but can go as low as $-30°\mathrm{C}$). Note the striking asymmetry of the minimum and maximum temperature profile (asymmetric envelopes).

The temperature amplitude ΔT is attenuated exponentially with depth z (Fig. 6c) proportional to $\exp\{-1.083z\}$. Looking at sub-daily resolution, AL temperature showed a daily course without time lag down to $-2.9\,\mathrm{m}$, only with attenuated amplitudes (Fig. 6c). Specific humidity gradients (Fig. 6d) averaged over days–weeks were parallel to the temperature gradients because the AL is most often close to saturation. Exception were the summer 2022 dry spells that dried out the AL.

17

5.2 k_{eff} from heat flux plate and pyrgeometer measurements

The direct heat flux plate Q_{HFP} and pyrgeometer Q_{CGR3}^{rad} measurements give an overview of flux magnitudes and seasonality. The measured heat fluxes Q_{HFP} and Q_{CGR3}^{rad} are within ± 20 W m^{-2} on daily average (Fig. 7). The downward ($Q_{\text{HFP}} > 0$) flux into the block where the HFP/1 is placed on (warming, positive sign) is strongly correlated with the net radiation in the

385 instrumented cavity ($Q_{\text{CGR3}}^{rad} > 0$) on an hourly and daily timescale (Figs. 7, 8a, ①), with $Q_{\text{HFP}} = 0.7\,Q_{\text{CGR3}}^{rad} + 0.7$ W m^{-2} ($R^2 = 0.9$) during the thaw season. The scatter decreases with increasing averaging time (shown from hourly to daily). The two measurements systematically deviate, since the HFP/1 measures the heat flux locally whereas each pyrgeometer integrates hemispherically (with a cosine response) over the cavity surface (REV uncertainty), in addition to the instrumental uncertainty (HFP resistance error of max. 20%). To show the non-radiative fluxes ('deviation') as time series in Fig. 7a and as a histogram

390 in Fig. 7b, we subtract the correspondingly scaled $0.7\,Q_{\text{CGR3}}^{rad}$ from Q_{HFP}. In contrast, the upward Q_{HFP} fluxes (cooling) are mainly by non-radiative fluxes (the deviation term). Upward Q_{HFP} fluxes tend to increase with negative AL air temperature gradients (shown by the colours in Fig. 8a), but are insensitive to Q_{CGR3}^{rad}. The daily averages hide regular diurnal fluctuations and large, but infrequent hourly outliers within ± 30 W m^{-2} (not shown).

The circled numbers ①–④ introduced in Fig. 6 are marked in Fig 7 (Table 3): Heat fluxes during the thaw season are

395 $5-15$ W m^{-2} downwards (①). In winter 2021–2022, heat fluxes were small (≤ 2 W m^{-2}; ②) beneath a closed snow cover when the snow height h_S exceeds 60 cm (measured on a windswept rock-glacier ridge). In the snow-poor winter 2021–2022, Q_{HFP} and Q_{CGR3}^{rad} are episodically anti-correlated, i.e., the downward net radiation increased with rapid cooling (Dec 2021–Feb 2022, ③). Strong cooling occurred in summer and in autumn (Sep–Oct 2020, Oct 2021, Sep 2022; ④) during the passage of cold weather fronts. Strong non-radiative heat input occurred in spring (⑤).

400 The control on Q_{CGR3}^{rad} by the AL air temperature gradient that can be inferred from Fig. 8a is also shown in Fig. 9a. Daily average in-cavity net long-wave net radiation Q_{CGR3}^{rad} during the thaw seasons is strongly correlated with the vertical AL air (!) temperature gradient in the cavity, although the cavity is small enough that the air in the cavity is transparent to long-wave radiation and does not participate in the radiative heat transfer. The pyrgeometer 'sense' the rock surface temperatures, in turn controlled by the heat conduction within the blocks. Linear regressions of daily average values yield

405 $Q_{\text{CGR3}}^{rad} = 3.0\,(\Delta T_a / \Delta z) + 0.26$ W m^{-2} with $R^2 = 0.957$ for summer 2021, and $Q_{\text{CGR3}}^{rad} = 3.8\,(\Delta T_a / \Delta z) - 0.45$ W m^{-2} with $R^2 = 0.965$ for summer 2022. The constant of proportionality in $Q_{\text{CGR3}}^{rad} = k_{\text{eff}}(\Delta T / \Delta z)$ is an effective thermal conductivity (cf. Eq. 16, Sects. 4.5.1, 6.2). The Q_{CGR3}^{rad}–dT_{al}/dz relation differs for the two thaw seasons 2021 and 2022. Since the relation between Q_{HFP} and Q_{CGR3}^{rad} is identical for both summers (Fig. 8a), the difference must come from the temperature gradient rather than the pyrgeometer measurements.

410 Zooming in to sub-daily resolution reveals a hysteresis pattern. At hourly resolution, the near-surface HFP/2 heat flux is much more strongly controlled by the instantaneous AL air temperature gradients rather than by Q_{CGR3}^{rad} (Fig. 8b). On the 'cavity floor' at greater depth, the overall near-linear Q_{HFP}–Q_{CGR3}^{rad} relation is maintained, despite some scatter in the hourly values (Figs. 9a, 8a). Plotting hourly values of a clear summer day (July 15, 2022, as an example in Fig. 9a) reveals a clockwise
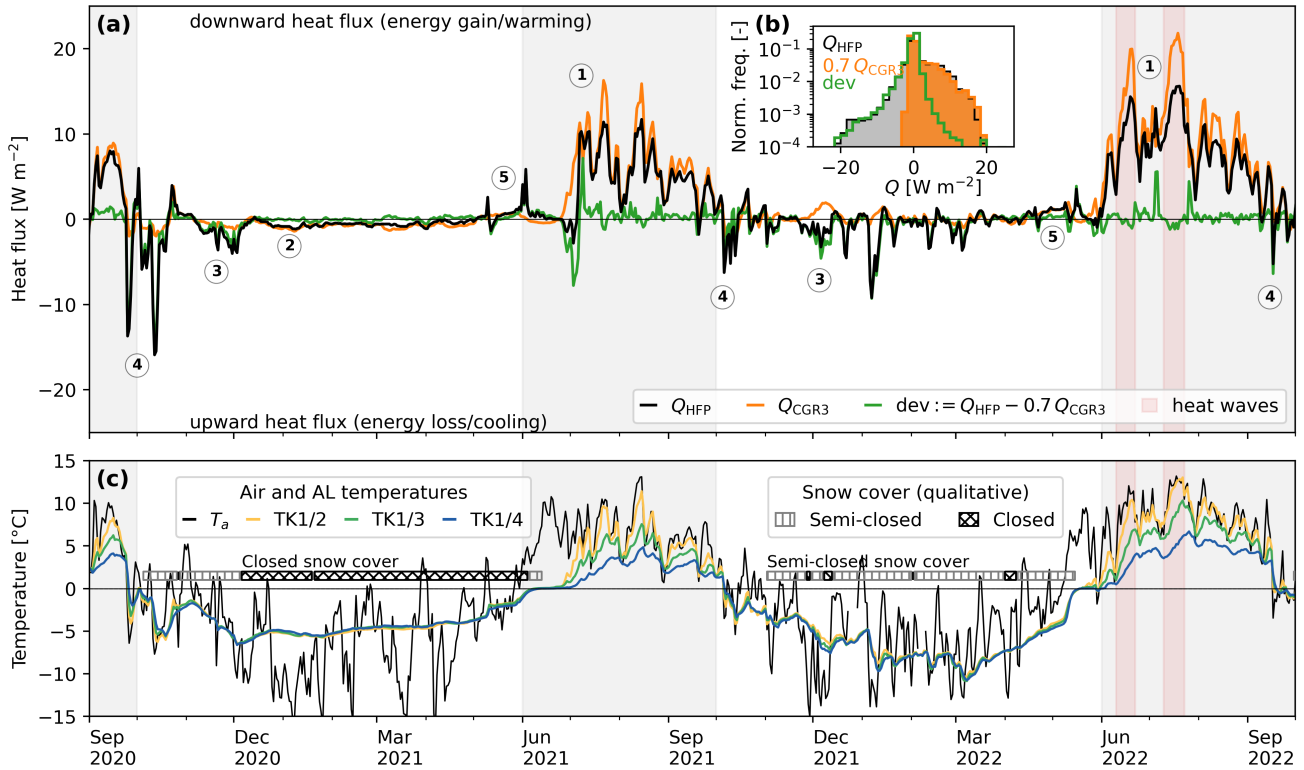
Figure 7. (a) Heat flux measured by the heat flux plate HFP/1 at the cavity floor Q_{HFP}, net AL long-wave radiation measured by the pyrgeometer pair Q_{CGR3}^{rad}, and the deviation $Q_{\text{HFP}} - 0.7 Q_{\text{CGR3}}^{rad}$ (daily averages). Positive flux is downwards into the rock slab. The circled numbers ①–⑤ refer to Table 3 and are detailed in the text. The snow cover is classified as 'semi-closed' (convective exchange through snow funnels) or 'closed' (little convective AL–atmosphere exchange) (Amschwand et al., 2023). Inset **(b)** Normalized histogram of the daily average fluxes. Downward fluxes (negative) are mainly conductive/radiative ($Q_{\text{HFP}} > 0$ is congruent with $0.7 Q_{\text{CGR3}}^{rad}$; Fig. 8a), upward fluxes (positive) are mainly non-conductive/convective ($Q_{\text{HFP}} < 0$ is congruent with the deviation). **(c)** Air and AL temperatures and snow cover status (closed/semi-closed).

hysteresis that mainly comes from diurnal cycles of Q_{CGR3}^{rad} and $(\Delta T_a / \Delta z)$ that are out of phase (black points, midnight value marked by the red cross). Air temperature leads and net long-wave radiation follows. A similar hysteresis is shown in Fig. 8a.

Daily average in-cavity net long-wave radiation Q_{CGR3}^{rad} is correlated with the 2-m air T_a and the radiometric ground surface temperature T_s (derived from the PERMOS outgoing long-wave radiation, Amschwand et al. (2023)) as long as T_s is above the freezing point (Fig. 9b). The correlation slightly improves for T_s of the *previous day* rather than T_s of the same day (2022 R^2 increases from 0.723 to 0.786). Also the Q_{CGR3}^{rad}–T_s relation differs for the two thaw seasons 2021 and 2022. Below 0°C, the Q_{CGR3}^{rad}–T_s relation breaks down and radiative fluxes remain small, within $\pm 2 \, \text{W m}^{-2}$, with flux magnitude and direction that is independent of the outside air or surface temperatures.
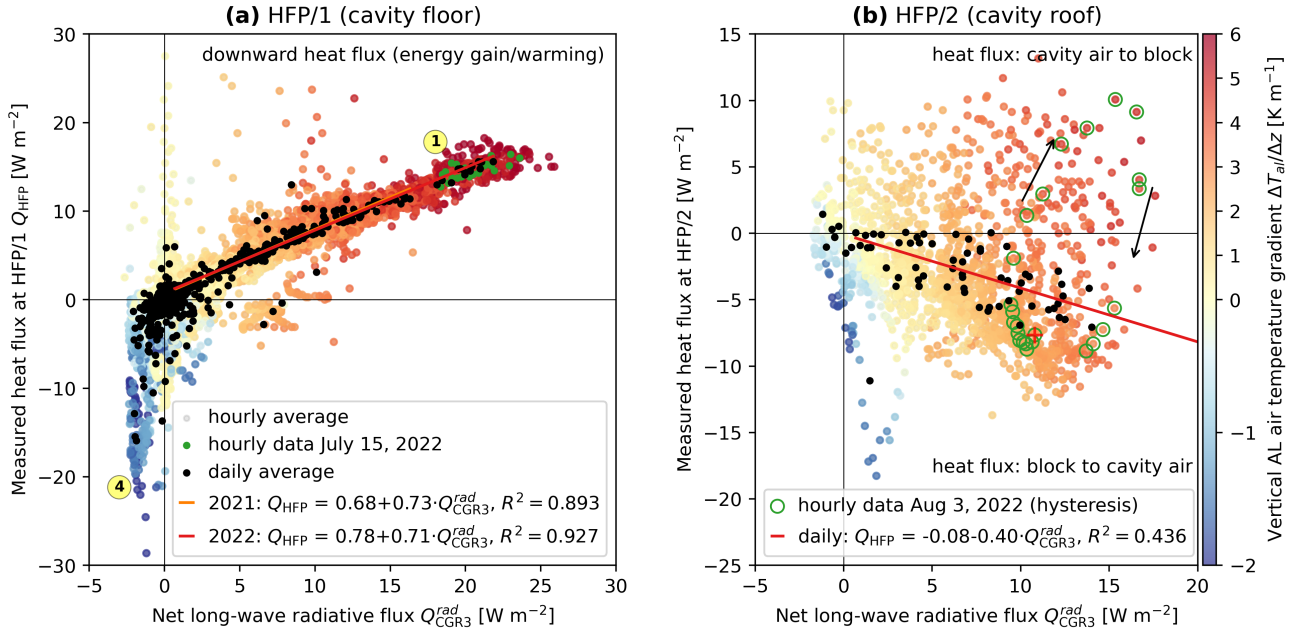
Figure 8. Relation between the two measured plate heat fluxes Q_{HFP} and net long-wave radiation Q_{CGR3}^{rad}. **(a)** HFP/1, cavity floor. ① During the thaw seasons at stable AL air temperature gradient and $Q_{\text{CGR3}}^{rad} > 0\,\text{W m}^{-2}$, the two heat fluxes are strongly correlated at both hourly and daily timescales ($Q_{\text{HFP}} \propto Q_{\text{CGR3}}^{rad}$ with $R^2 = 0.9$). ④ The relation breaks down at unstable gradients, where $Q_{\text{HFP}} \propto (\Delta T/\Delta z)$. The circled numbers ① and ④ refer to Table 3. **(b)** HFP/2, cavity roof (sign convention: positive means into the block). Hourly and daily fluxes do not coincide and show a diurnal hysteresis (HFP/2 measurement available only after Jul 26, 2022).

Assuming steady state conditions (discussed in Sect. 6.1.1), an effective thermal resistance R_{eff} [K m^2 W^{-1}] of the AL can be derived from the observed linear temperature profile (Fig. 9a) and the linear Q_{CGR3}^{rad}–T_s relation (Fig. 9b; e.g., Nakawo and Young (1981, 1982); Kayastha et al. (2000); Mihalcea et al. (2006); Fujita and Sakai (2014); Rounce and McKinney (2014)),

$$R_{\text{eff}} := \frac{h_{al}}{k_{\text{eff}}} = \frac{T_s - 0°\text{C}}{Q_{\text{CGR3}}^{rad}}, \tag{18}$$

425

where h_{al} is the AL thickness. The inverse thermal resistance corresponds to thermal conductivity normalized by AL thickness. Both formulations yield similar values of $R_{\text{eff}} \approx 0.8-1.0$ K m^2 W^{-1} (Fig. 9).

5.3 Thaw-season apparent thermal diffusivity κ_a

The apparent thermal diffusivity κ_a (calculated from daily AL temperatures as outlined in Sect. 4.5.2, Eq. 17) during the 2021 and 2022 thaw seasons varies over two orders of magnitude between 2×10^{-5} and 2×10^{-7} m^2 s^{-1} and includes negative values (Fig. 10). The thaw-season log-mean $\bar{\alpha}_a$ is 2.3×10^{-6} m^2 s^{-1}. κ_a is largest at unstable or near-isothermal air stratification (1.9×10^{-5} m^2 s^{-1} at $\Delta T/\Delta z < 0.5$ K m^{-1}), has the largest scatter at weakly–moderately stable conditions

430

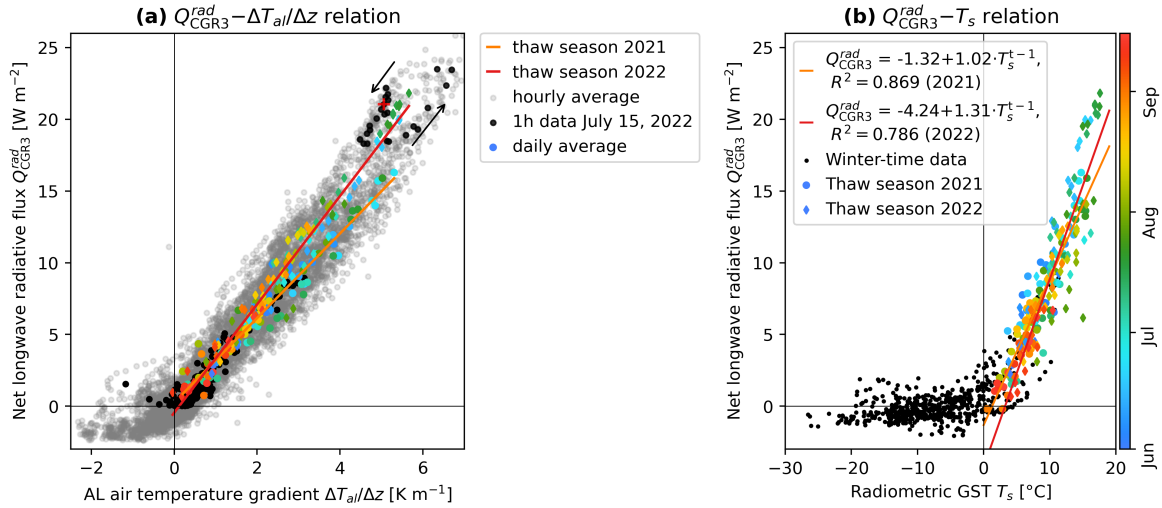**Figure 9. (a)** Long-wave net radiation Q_{CGR3}^{rad} vs. vertical AL air temperature gradient $\mathrm{d}T_{al}/\mathrm{d}z$. Daily averages are highly correlated (2021: $R^2 = 0.957$, 2022: $R^2 = 0.965$), with slopes (k_{eff}) of 2.9 and 3.8, respectively (Eq. 16). Hourly values show a hysteresis. **(b)** Long-wave net radiation vs. radiometric ground surface temperature (rGST) of the previous day ($R^2 = 0.786$) during the thaw season.

$(0.5\,\mathrm{K\,m^{-1}} < \Delta T/\Delta z < 4\,\mathrm{K\,m^{-1}})$, and approaches $\kappa_a^0 = 9.6 \times 10^{-7}\,\mathrm{m^2\,s^{-1}}$ at strongly stable air stratification ($\Delta T/\Delta z > 4\,\mathrm{K\,m^{-1}}$), where turbulence is suppressed and convective heat transfer is minimal. We also derived κ_a using the amplitude
435   method (Hinkel et al., 1990; Vonder Mühll and Haeberli, 1990; Harris and Pedersen, 1998; Juliussen and Humlum, 2008), where we fitted $\kappa_a^{\Delta T}$ to the amplitude of daily temperature variation (max−min) that is attenuated exponentially with depth (Fig. 6c). This $\kappa_a^{\Delta T} = (3.1 \pm 0.3) \times 10^{-5}$ based on hourly TK1 temperature values is strongly biased to convection. Since hourly AL *air* temperatures are not necessarily representative of the AL thermal regime (the blocks take longer than one hour to thermally equilibrate), we discard this estimate.

440   **5.4   Sub-surface airflow**

Sub-surface AL airflow speeds (Fig. A1) differ seasonally in terms of (i) spatial pattern (depth of maximum speed) and (ii) temporal pattern (timing of diurnal oscillations). In the 'open', snow-free summer season, airflow is detected by all wind speed sensors with maximum airflow speeds near the surface of up to $20\,\mathrm{cm\,s^{-1}}$. Airflow speed generally decreases with depth, and there is a strong, regular daily cycle with its speed peak in the afternoon and calm nights (Fig. 11b), in phase with the insola-
445   tion. This diurnal pattern is shared by all WS sensors close to the surface (Amschwand et al., 2023). In winter, the amount of snow controls the strength of the air circulation and possibly also the airflow pattern/air pathways. Under a thick snow cover in winter 2020–2021, AL airflow is weak and beneath the level of detection at all sensors and depths. One WS/5 (wind hole near the surface) was completely snowed in. In the snow-poor winter 2021–2022, AL circulation resumes in December 2021 one month after the onset of the snow cover. Our measured air circulation is most vigorous and persistent near the surface in a
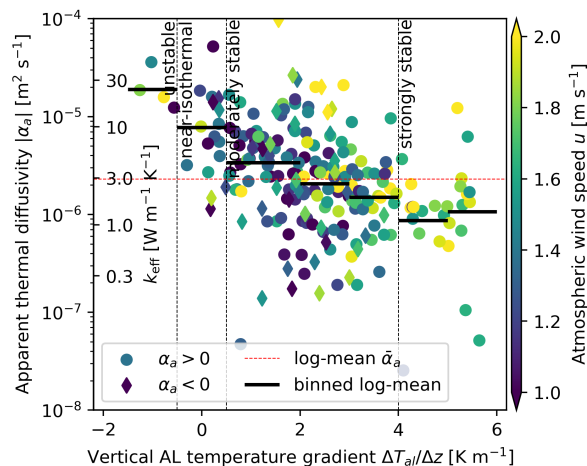
Figure 10. Apparent thermal diffusivity κ_a during the two thaw seasons 2021 and 2022 ($T_{al} > 1°C$) calculated from daily average AL temperatures in the instrumented cavity (TK1/3 at 1.6 m depth; Eq. 17).

450 rock-glacier furrow, a topographic depression (WS/6 in Fig. A1). The timing of diurnal oscillation is opposite to the 'summer mode' with the diurnal peak airflow speed in the night and calm days, however much less strong and regular as in summer. Slow changes over a timescale of days is more important, apparently in response to outside forcing (temperature, wind speed).

The AL airflow speed measurements reveal the two driving forces, buoyancy forces and wind shear, conditioned by the depth beneath surface and the snow cover (Figs. A2, 12). Fig. 11 shows a data illustration of three different air circulation modes that

455 occurred during the autumnal cooling 2020, (i) shallow ventilation of the stably stratified AL air column, (ii) buoyancy-driven Rayleigh ventilation, and (iii) wind-forced mixing of the isothermal, labilized air column.

The deepest WS/1 (-2.1 m, Fig. 3) shows the highest airflow speeds at unstable air density stratification (Rayleigh ventilation; Fig. 12a) and isothermal cavity at high outside wind speeds (wind-forced convection). Atmospheric wind sets the labilized air column down to the cavity base in motion. At stable AL air temperature gradients, airflow speed is overall low, but even

460 then, airflow speeds tend to be higher under high atmospheric wind speed. The effect of wind-forced convection is weak, but detectable in the wide instrumented cavity down to 2 m depth. Note the striking similarity with Fig. 8a.

Under snow-free conditions, the near-surface WS/6 airflow speed (shown as an example in Fig. 12c) is overall higher, increases with atmospheric wind speed, and is insensitive to the (anyway mostly stable) vertical temperature gradient (wind-forced ventilation). The thicker the snow cover and the stronger the decoupling between AL and atmosphere (AL–atmosphere

465 coupling in Amschwand et al. (2023)), the more important density contrasts become to drive the air circulation (buoyancy-driven ventilation), however at overall lower airflow speeds (Fig. 12b).

Average airflow speed as measured in the instrumented cavity did not decay with depth as expected (cf. Evatt et al. (2015)). The lowermost WS/1 mounted in a narrow constriction (Fig. 3, Table 2) showed higher wind speeds and responded more sensitively than the WS/2 in the more spacious mid-cavity (Venturi effect).
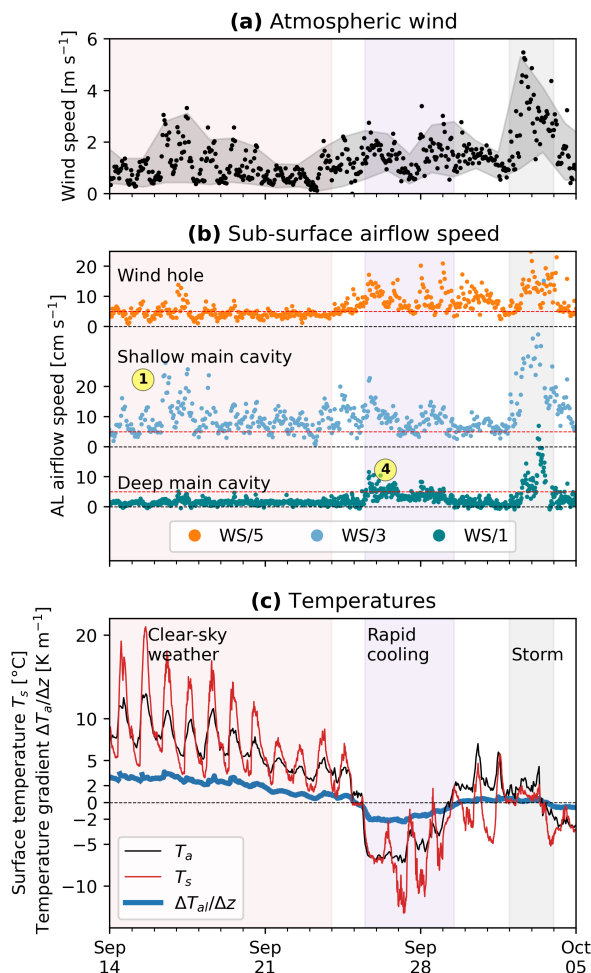
Figure 11. Zoom-in to the autumnal cooling in 2020 that illustrates the different air circulation modes in the coarse-blocky AL. Above-surface meteorological conditions (insolation and surface temperature, wind speed) and the ground thermal regime (vertical temperature gradient) interact to produce characteristic air circulation modes. **(a)** Atmospheric wind speed. **(b)** Strong diurnal surface heating with shallow *wind-forced ventilation* (WS/3) is characteristic for clear summer days (①). Stable air stratification allows only weak circulation in the deep cavity (WS/1) despite occasionally strong winds. Rapid surface cooling destabilizes the air column and produces buoyancy-driven circulation (Rayleigh ventilation ④). Vigorous mechanical mixing of the isothermal, labile air column by strong winds rarely occurs because it requires an isothermal air column under snow free conditions. **(c)** Temperatures. (The circled numbers ① and ④ refer to Table 3).

5.5 Seasonal AL ice melt

The ground-ice table (GIT) as observed in a rock-glacier furrow deepened by $60\,\mathrm{cm}$ during the thaw season Jun–Sep 2022, grew by $30\,\mathrm{cm}$ in winter 2022–2023, and deepened again by (at least) $40\,\mathrm{cm}$ in Jul–Sep 2023 (Fig. 13a, b). The amount of ice lost
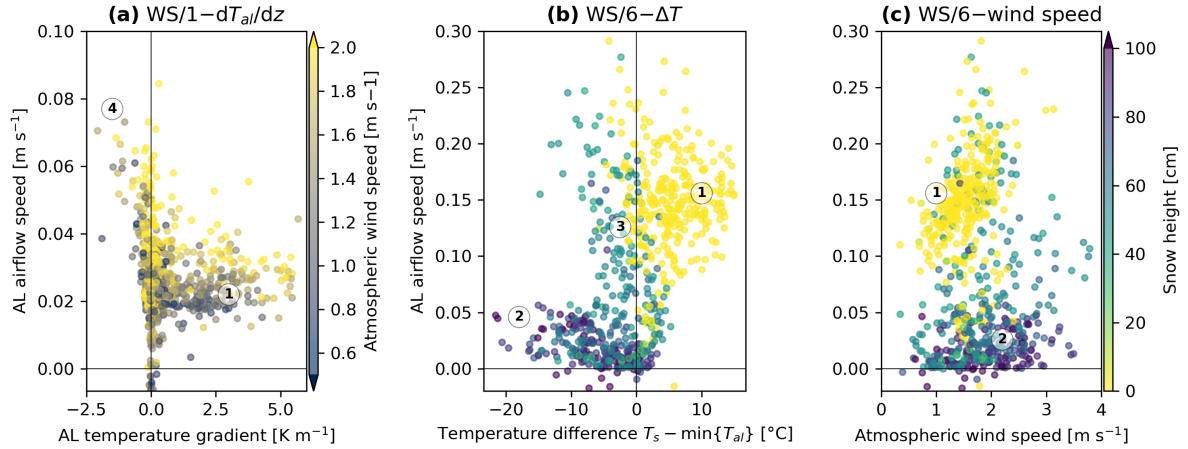
Figure 12. Drivers of ventilation. **(a)** Ventilation at depth (WS/1) is primarily buoyancy-driven (④). At stable stratification (positive temperature gradients), airflow speeds are low but enhanced by the atmospheric wind (①). **(b, c)** The near-surface ventilation (WS/6) transitions from mainly wind-driven (①) to buoyancy-driven circulation with increasing snow height (②, ③). The circled numbers ①–④ refer to Table 3.

due to melt is equivalent to a heat flux $\bar{Q}_m$ of ~ 10 W m^{-2} on average during the 2022 thaw season (porosity $\phi_{al} = 0.4 \pm 0.1$ in Eq. 7, Fig. 13c). The thaw rates accelerate and decelerate with a peak in mid-July, proportional to the surface temperature

475 $\dot{\zeta} \propto T_s$ throughout the thaw season (Fig. 13c). Thaw rates are independent of the time elapsed since onset of the thaw season, no hysteresis can be observed. This has two important implications: First, this justifies the two-layer Stefan equation (Eq. 13), because the one-layer Stefan equation (Eq. 11) predicts $\dot{\zeta} \propto \sqrt{t}$, with thaw rates rapidly slowing down as the thaw front recedes away from the surface. The critical parameter is h_1 that represents the ice-poor overburden (h_1 "flattens out" the square root relation). Second, it makes a temperature index model with a constant f_m applicable.

480 5.5.1 Temperature index model

From the 7 ablation observations in summer 2022 (one outlier removed), we get the empirical relation between ablation rate and the radiometric ground surface temperature (Eq. 9) of

$$\Delta\zeta/\Delta t = -0.008 - 0.053\,T_s \text{ [cm day}^{-1}], \tag{19}$$

with $R^2 = 0.712$ (Fig. 13c). Similar correlations exist to 2-m air temperature T_a, $\Delta\zeta/\Delta t = -0.012 - 0.075\,T_a$ ($R^2 = 0.726$),

485 a nearby UTL temperature (UTL #2735, Fig. 3) ($R^2 = 0.384$), or the difference $T_a - \text{UTL}_{2735}$, $\Delta\zeta/\Delta t = -0.122 - 0.140\,\Delta T$ ($R^2 = 0.901$; shown in Fig. 13a), or $T_s - \text{UTL}_{2735}$ ($R^2 = 0.798$). The empirical relation from the 2022 measurements slightly overestimates the 2023 ablation rates, but is still within a plausible range (Fig. 13b). Converting Eq. 19 from ablation rate to melt energy flux Q_m (Eq. 7) yields $Q_m = -0.1 + (0.7 \pm 0.2)T_s$ [W m^{-2}], which agrees with the effective thermal resistance R_{eff} of $0.8-1.0$ K m^2 W^{-1} derived from the radiation measurements (Eq. 18, taking $Q_m = Q_r$). We emphasize that the lowering
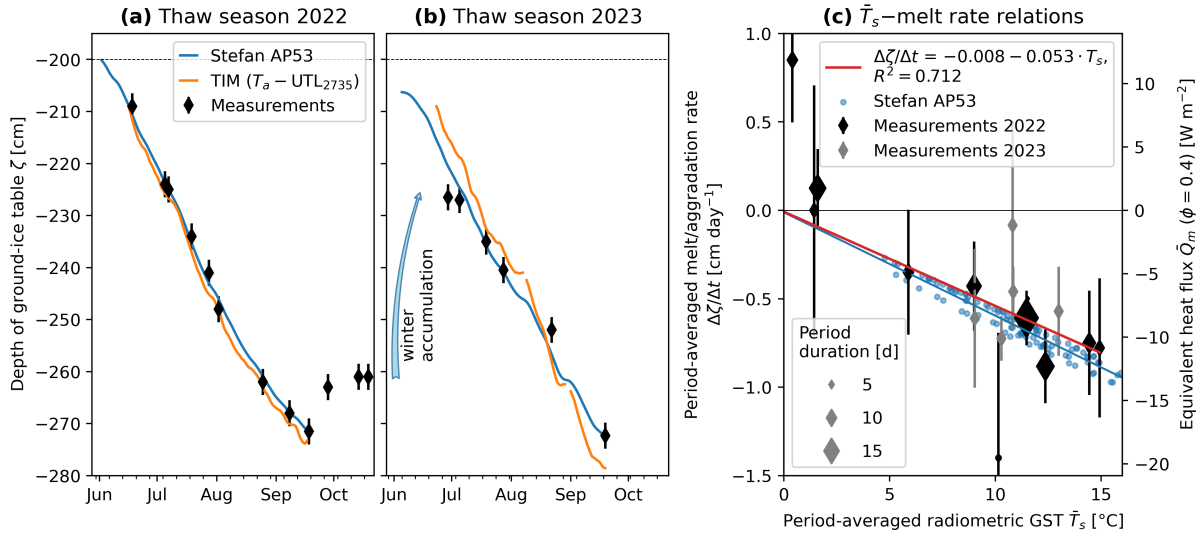
Figure 13. Observed vertical changes in the ground-ice table in thaw season **(a)** 2022 and **(b)** 2023 with seasonal accretion and ablation. Measurement uncertainty ~ 5 cm. Ablation is simulated with the Stefan model (Aldrich and Paynter (1953), Eq. 13, Fig. 4) and the temperature index model (TIM, Eq. 9). **(c)** The ground-ice melt rates are correlated with the ground surface temperature.

490 of the ground ice table is observed within the blocky AL, i.e. needs to be multiplied by porosity ϕ to obtain an ablation in the glaciological sense.

5.5.2 Stefan parameterisation

With $k_{\text{eff}} = 3.0 \pm 0.3$ W m^{-1} K^{-1} a priori derived from our measurements (Sect. 5.2) and $f_2 = \phi_{al} = 0.4$ (saturation), the best-fit parameters for Eq. 13 are $\hat{f}_1 = 0.01$ and $\hat{h}_1 = 3.0 \pm 0.25$ m (Fig. 13a). This relation based on 2022 data predicts the 495 2023 ablation rates well. The estimated $\hat{h}_1$ is 50% thicker than the actual distance to the initial ground-ice table (~ 2 m), but still plausible given the rough terrain and input data uncertainties: The "excess" overburden/insulation might compensate for the likely too high forcing thaw index $I_t(T_s)$ in the shaded furrow, as $I_t(T_s)$ is derived from the PERMOS outgoing long-wave radiation $L^{\uparrow}$ on a sun-exposed plateau.

6 Discussion

500 We first discuss the AL heat fluxes and the two parameterisations of the ground ice melt (Sect. 6.1). Then, motivated by the seasonality imposed by the snow cover (AL–atmosphere connectivity; Amschwand et al. (2023)) as shown by the AL temperature envelopes (Fig. 6a) and the measured heat fluxes (Fig. 7), we address heat transfer processes and the AL effective thermal properties in the thaw season (Sect. 6.2) and in winter (Sect. 6.3). Table 3 provides an overview on how the seasonally varying dominant heat transfer processes are shown by our data.

Table 3. Temperature profiles, heat fluxes and airflow patterns at characteristic weather patterns and snowpack conditions (①–⑤) is referred to in the text and figures).

#	Conditions	Temperature profile and Rayleigh number (Fig. 6)	Heat fluxes (daily averages) (Figs. 7, 8, 9)	Air circulation modes (Figs. 11, 12, 15, 16)
On seasonal timescale (over weeks–months)				
①	Thaw season	Mostly[a] near-linear profile (daily timescale), positive gradient/stable	$Q_{\mathrm{HFP}} \propto Q_{\mathrm{CGR3}}^{rad} \propto \mathrm{d}T_{al}/\mathrm{d}z$, $5-15$ W m^{-2} downwards, $Q_{\mathrm{CGR3}}^{rad} \propto T_s$	*Wind-forced convection* enhances radiative–conductive heat transfer (Fig. 15d)
②	Winter stagnant/ closed snow cover	Near-linear profile, isothermal or weakly unstable gradient, slowly evolving	$Q_{\mathrm{HFP}} \approx Q_{\mathrm{CGR3}}^{rad}$, < 2 W m^{-2} upwards	No convective AL–atmosphere coupling
③	Winter semi-closed snow cover	'Bulged' profile, fluctuating in time	$Q_{\mathrm{HFP}} > Q_{\mathrm{CGR3}}^{rad}$, often anti-correlated, $2-10$ W m^{-2} upwards	*Cold-air infiltration* through semi-closed snow cover (snow funnels; Fig. 16)
Short-lived events (hours–days)				
④	Convective overturning	Unstable (Ra $>$ Ra$_c$), rapidly changing (transient)	$Q_{\mathrm{HFP}} \gg Q_{\mathrm{CGR3}}^{rad}$, large: $20-30$ W m^{-2} upwards	*Rayleigh ventilation* (dominant heat transfer mode)
⑤	Water refreezing	Rapid temperature rise towards 0°C at all AL depths	$Q_{\mathrm{HFP}} > Q_{\mathrm{CGR3}}^{rad}$, $4-8$ W m^{-2} downwards	

[a] Exceptions are dry-hot weather spells (Fig. 6b) or during the passage of weather fronts.

6.1 AL energy budget and melt parameterisations

6.1.1 Thaw-season heat partitioning

Fig. 14 shows the cumulative heat uptake (denoted by $\Sigma_t(\cdot)$) during the two thaw seasons 2021 and 2022. At the onset of the thaw season which coincides with the disappearance of the snow cover, the AL exits the zero-curtain phase near-isothermal at 0°C. This is the thermodynamic reference level in Fig. 14, hence the sensible heat H_{al}^{θ} is zero at the onset and end. During the thaw season, the AL is a heat sink that absorbs roughly 10% of the surface net radiation Q^* (Fig. 14), hence $Q_G \approx Q^*/10$ (Amschwand et al., 2023), and that in both thaw seasons until mid/end August. With approximately constant heat uptake rates, the date of thaw season onset is the primary control on the total cumulative thaw-season heat uptake, in turn controlled by the total winter precipitation, spring weather, and melt-out date. After the snow-poor winter 2021–2022, the thaw season 2022 started one month earlier than in 2021 and received almost twice the amount of heat, 93.7 MJ m^{-2} instead of 52.1 MJ m^{-2}, although the thaw season lasted only 15 days longer (Table 4).

The available heat from the surface ground heat flux Q_G is partitioned into sensible heat storage changes ΔH_{al}^{θ}, latent heat storage changes Q_m, and conducted into the permafrost body beneath the AL Q_{PF} (Eq. 3, Table 4). On thaw-season average,

Q_G is largely ($\sim 70\%$) spent on melting ground ice. Hence, *latent heat effects contribute substantially to the thermal buffering* — this is a mechanism that renders rock glaciers climate-resilient, provided that seasonal accumulation of superimposed

520 ice compensates for its melt. Otherwise, permafrost ice melts, leading to AL thickening and ultimately permafrost degradation. Roughly $\sim 20\%$ of Q_G is absorbed by the coarse-blocky AL as sensible heat storage H_{al}^{θ}. The heat conducted into the permafrost body beneath the AL Q_{PF} amounts to ~ 10 MJ m^{-2} ($\sim 10\%$). If that amount of heat is converted to permafrost ice melt, it would translate to $30-60$ kg m^{-2} or a subsidence of $3-7$ cm yr^{-1} (assuming massive permafrost ice (Vonder Mühll and Haeberli, 1990)). It is consistent with the observed increase in AL thickness of 1 m in the years 2010–2018 or

525 ~ 12 cm yr^{-1} (Noetzli et al., 2019) (the permafrost is "warm" at temperatures of $\geq -3°$C). The cumulative rain heat flux Q_{Pr} (Eq. 5) is 11 MJ m^{-2} in the cool-wet summer 2021. Q_{Pr} is a small flux compared to Q_G in 2022 ($5-10\%$ considering the rainfall undercatch), but not in 2021 (20%), and is similar to Q_{PF}.

Table 4. Thaw-season average (avg) and cumulative total (cum) heat partitioning.

	Thaw season 2021		Thaw season 2022	
duration	95 days		110 days	
[MJ m^{-2}]	avg	cum	avg	cum
Q^* (SEB)	444	753	633	1136
Q_G (SEB)	37.3	52.1	64.9	93.7
$Q_r{}^a$	32.0	54.6	51.6	94.4
H_{al}^{θ}	9.5	0.0	20.7	0.0
Q_{PF}	4.0	7.4	7.3	12.7
Q_{Pr}	6.9	11.0	1.5	4.7
dev$_{al}{}^b$	30.7	55.7	38.4	85.7
Q_m (AP53)^c	31.4	55.9	52.7	88.5
Q_m/Q_G	0.84	1.07	0.81	0.94
Q_G/Q^*	0.08	0.07	0.10	0.08

$^a Q_r$ is the pyrgeometer measurement Q_{CGR3}^{rad}. ^{b} AL energy budget deviation dev$_{al} := Q_G + Q_{Pr} - H_{al}^{\theta} - Q_{\mathrm{PF}}$. ^{c} Ablation parameterised via Eq. 13 and converted to Q_m via Eq. 7. The 2021 ablation where no observation are available is estimated with the 2022 parameters and the 2021 forcing T_s.

The thaw season is divided in two phases, an AL heating and a ground ice melting phase. Initially, the ice-poor shallow AL is heated from the surface downwards ($H_{al}^{\theta} > \Sigma_t Q_m$). However, the uptake of sensible heat saturates after $2-3$ weeks because

530 the AL base is kept at the melting point and the surface temperature T_s has an upper limit: The surface energy balance (SEB) responds to higher T_s with larger turbulent fluxes that exert a cooling effect (heat export into the atmosphere; Amschwand et al. (2023)). The sensible heat uptake on Murtèl reaches $\sim 20-25$ MJ m^{-2} (peak uptake $(H_{al}^{\theta})^{max}$ during the July 2022 heat wave
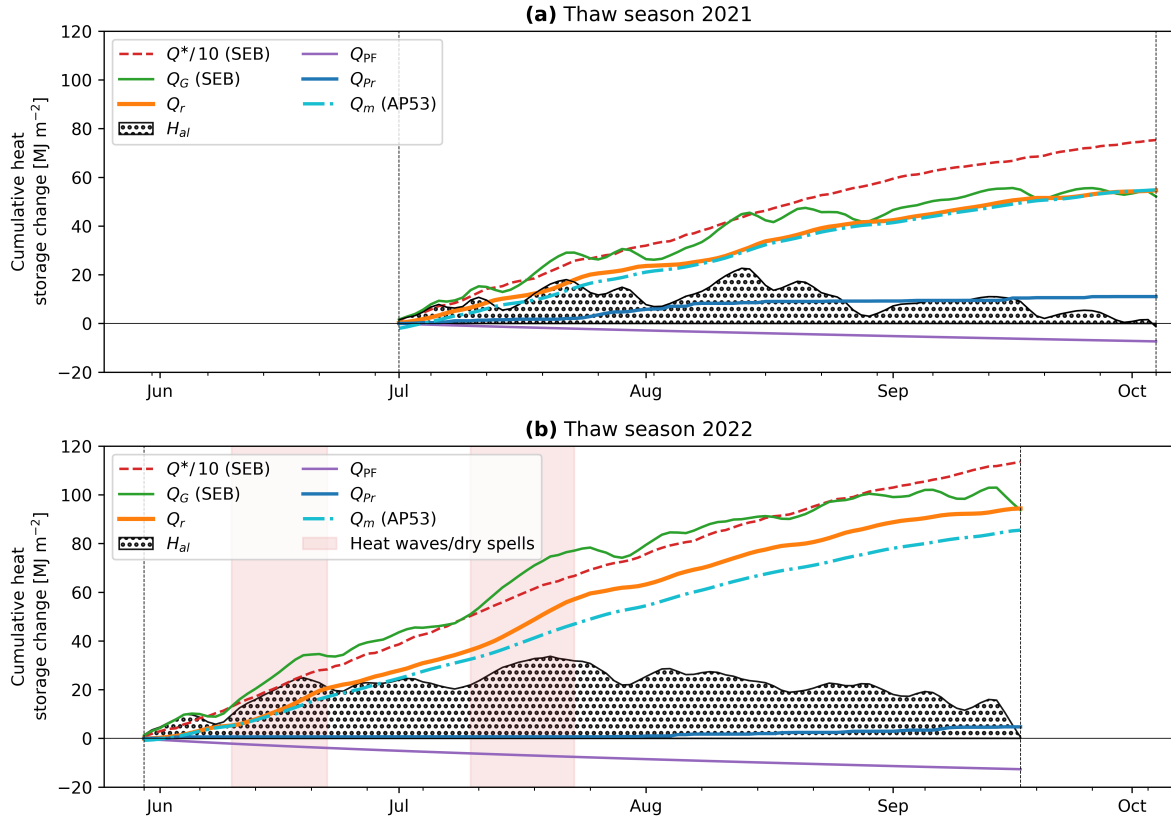
Figure 14. Heat uptake and partitioning during the **(a)** 2021 and **(b)** 2022 thaw seasons. The heat supplied to the AL, primarily controlled by the thaw season onset, is mostly absorbed by melting ground ice Q_m.

of $35\,\mathrm{MJ\,m^{-2}}$). Once this threshold storage is reached, the sensible heat storage changes little (even slowly loses heat in late summer), and the heat goes mainly into ice melt ($\Sigma_t Q_m > H_{al}^\theta \approx \mathrm{const.}$). In this second phase, the near-surface AL does still

535   warm and cool in response to the atmospheric forcing, but the sensible heat storage changes ΔH_{al}^θ are small compared to the total heat uptake $\Sigma_t Q_G$. Hence, over timescales of a few days, the AL is not far from a quasi-steady state, and concepts like the effective resistivity R_{eff} (Eq. 18) and the Stefan equation (Eq. 10) are approximately valid.

6.1.2 Seasonal ground-ice melt rates

The observed 2022 ground ice melt Q_m in the rock glacier furrow agrees within $3\,\mathrm{MJ\,m^{-2}}$ with the melt dev_{al} calculated

540   from the energy budget in the nearby instrumented cavity (Eq. 3; Fig. 14, Table 4). This is important: The melt estimated from the energy budget deviation (dev_{al} sensu Scherler et al. (2014)) and the direct ablation observations concur for the thaw season 2022 where the energy–ablation data set is complete. Systematic ablation observations were not performed in 2021.

Our (to our knowledge unique) data set of seasonal ground ice changes provides a statistical relation necessary for a temperature index model of seasonal melt in rock glaciers (Eq. 9). The best correlation is achieved with the 'local' air temperature

545   difference $(T_a - \mathrm{UTL}_{2735})$ (Fig. 13a). The temperature index model successfully simulates the thaw (Fig. 13a, TIM). However, the prize to pay is a local miniature temperature logger whose measurements are strongly sensitive to micro-meteorological position and depth beneath ground surface, due to the strong vertical temperature gradients (Fig. 6b) (Staub et al., 2017; Gubler et al., 2011). Our 10 UTL measurements suggest that such a statistical degree-day relation with near-surface AL temperatures is not transferable to other places even on the same landform. Hence, it is unclear how representative the statistically calibrated

550   melt factor $\hat{f}_m$ (Eq. 9) for different AL thermal properties (block size) and depths to the ground ice table is. The use of a temperature index model is limited by the unknown transferability of the empirical melt factor $\hat{f}_m$.

An alternative to the simple and parsimonious temperature index model is the more process-based Stefan model, where the key parameter effective thermal conductivity k_{eff} can be related to thermal AL properties/processes and constrained a priori (Sect. 6.2). Also, the initial depth h_1 to the ground ice table is accounted for. The Stefan model with two modifications

555   accounting for the insulating top layer and the sensible heat storage successfully simulates the cumulative seasonal ground ice ablation. Seasonal melt rates are proportional to ground surface temperature T_s (Fig. 13c) and independent of the time elapsed since onset of the thaw season. Our data set, although sparse, does not suggest a melt rate–surface temperature hysteresis that would result from decelerating thaw rates, $\mathrm{d}\zeta/\mathrm{d}t \propto (I_t)^{-1/2}$. This linear ζ–t relationship is the insulating effect of the ice-poor top layer (h_1 in Eq. 13) that slows down the thaw rates from the onset of the thaw season, hence the modified two-layered

560   Stefan equation.

Both used models, the Stefan model and the degree-day model, are compatible with our observations within their uncertainties simply because the two forcing variables, the surface temperature T_s and air temperature T_a (respectively), are correlated at the timescale of our ablation observations of several days. Useful findings to model ground ice melt rates are (i) the near-linear daily average temperature profiles under fair-weather conditions and (ii) the good correlation between radiometric surface tem-

565   perature T_s and the AL temperature gradient and, by consequence, the radiative–conductive downward heat flux (Fig. 9). This supports the Stefan model that links thaw rates to the surface temperature T_s (Sect. 6.2), potentially relates the sub-surface heat flux with remotely sensible surface properties via an effective thermal resistance R_{eff} (Nakawo and Young, 1981, 1982; Rana et al., 1997; Kayastha et al., 2000; Mihalcea et al., 2006; Fujita and Sakai, 2014), and resonates with the observed quasi-linear seasonal temperature profiles in the debris cover of Himalayan glaciers during the ablation season (defined equivalently

570   to the thaw season) (Conway and Rasmussen, 2000; Nicholson and Benn, 2006, 2013; Rowan et al., 2021), and organic-rich arctic soils (Hayashi et al., 2007). However, the Q_{CGR3}^{rad}–T_s relation and the Q_{CGR3}^{rad}–$\mathrm{d}T_{al}/\mathrm{d}z$ relation differ for the two thaw seasons 2021 and 2022 (Fig. 9), which implies that they are sensitive to the meteorological conditions and not only on the time-invariant debris properties. More in-situ observations and measurements are necessary to constrain the thermal properties of coarse-blocky AL and their spatial variation, including the role of moisture transfer and evaporation. So far, few direct

575   observations of seasonal ground ice changes in the hardly accessible AL of mountain permafrost landforms exist. Rist (2007) interpreted seasonal ground ice formation and melting of $\sim 10\,\mathrm{cm}$ in the ice-saturated AL base in a permafrost-underlain scree slope in the *Upper Engadine* (Switzerland). Related examples are Sawada et al. (2003); Sawada (2003) who monitored the

seasonal ground-ice table in a block field on *Mt. Nishi-Nupukaushinupuri* (Hokkaido, Japan) or Yoshikawa et al. (2023) on *Maunakea* (Hawai'i). Another route is via numerical modelling of the coupled heat and mass transfer. For example, the Murtèl

580 rock glacier exemplifies Renette et al. (2023)'s modelling scenario 'blocks only, drained', and our field observations largely support their model results of the seasonal evolution of the ground ice table.

6.2 Thaw-season heat transfer

Using an electrical resistance network as an analogue, we understand the heat transfer in the coarse-blocky AL as simultaneously and parallel acting radiative–conductive and convective processes, but with varying relative contribution to the total heat

585 flux Q_G (Sect. 4.2). We restrict the analysis to the AL in the thaw season (here defined by $T_{al} > 0°$C, unfrozen) to exclude latent heat effects. When does radiation–conduction, when does convection dominate the heat transfer? We propose a criteria based on the HFP/1 heat flux Q_{HFP}^{tot} and the CGR3-measured net long-wave radiation Q_{CGR3}^{rad}. We'll distinguish two cases:

1. The heat fluxes Q_{CGR3}^{rad} and Q_{HFP}^{tot} are correlated ($Q_{\mathrm{CGR3}}^{rad} \propto Q_{\mathrm{HFP}}^{tot}$), the cavity-integrated radiative heat flux Q_{CGR3}^{rad} agrees with the total heat flux Q_{HFP}^{tot} measured locally on the 'cavity floor' within the measurement uncertainties (instru-

590 mental and REV uncertainty). The radiative–conductive flux Q_r dominates and accounts for the total heat flux Q_G. This case occurs during most of the thaw season at stable temperature gradients (only *wind-forced convection*) or beneath a closed snow cover (Fig. 7 ①②).

2. The heat fluxes Q_{CGR3}^{rad} and Q_{HFP}^{tot} are not correlated ($Q_{\mathrm{CGR3}}^{rad} \not\propto Q_{\mathrm{HFP}}^{tot}$) and deviate substantially in magnitude or occasionally in direction: Convective heat flux dominates. This case occurs during unstable temperature gradients or beneath

595 a semi-closed snow cover (*buoyancy-driven convection*; Fig. 7 ③④). It also occurs on sub-hourly timescales when rainwater infiltrates (advective heat flux) or water refreezes (⑤).

6.2.1 Convection-enhanced apparent thermal diffusivity κ_a

The thaw-season log-mean $\bar{\kappa}_a = 2.3 \times 10^{-6}$ m^2 s^{-1} (Fig. 10) is consistent with the thaw-season averaged effective thermal conductivity $\bar{k}_{\mathrm{eff}} \approx 3$ W m^{-1} K^{-1} derived from the pyrgeometer measurements (Fig. 9a). κ_a and k_{eff} are related via Eq. 15.

600 For negative AL temperature gradients, k_{eff} can be as high as 30 W m^{-1} K^{-1}. Our κ_a value agree with published values for ventilated coarse-blocky material, but are generally $2-6$ times higher than for finer material of supra-glacial debris (Rowan et al., 2021) or cryic regosol (Table 5).

κ_a is primarily controlled by the AL air column stability (vertical temperature gradient $\Delta T_{al}/\Delta z$) – controlling the vigour of *buoyancy-driven convection*, and secondarily by atmospheric wind speed u – controlling the vigour of *wind-forced convection*

605 (Fig. 10) (Herz, 2006). Hence, the total, convection-enhanced apparent κ_a is as much determined by the time-variable meteorological conditions as by the debris-mantle properties and thus variable in time. κ_a is higher for cooling (upwards heat transfer) at unstable temperature gradients than for warming at stable temperature gradients. The Murtèl coarse-blocky AL functions as a 'thermal semi-conductor' (Guodong et al., 2007; Johansen, 1975; Herz, 2006): frequent, but less efficient radiative-conductive warming (downward heat transfer) is countered by only occasionally occurring, but highly efficient convective cooling (upward

610   heat transfer) (Figs. 7, 10). The 'thermal semi-conductor' effect combined with the large AL thickness results in a high thermal

resistance R_{eff} (Eq. 18), which is another mechanism that renders rock glaciers climate-resilient.
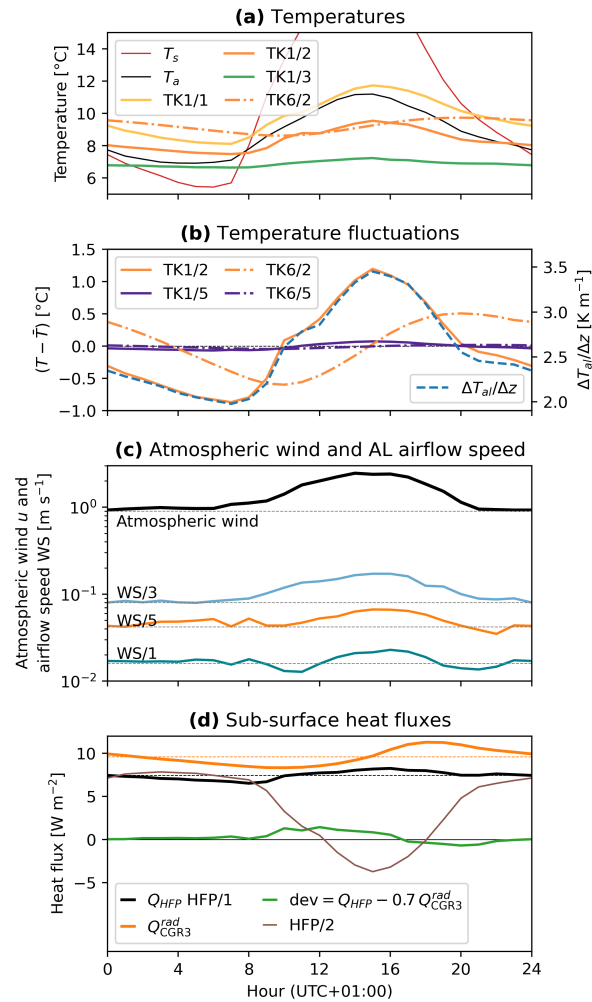

Figure 15. Evidence for wind-forced convection from sub-daily data: August 2022 hourly averages of **(a)** temperatures (T_s, T_a, AL air TK1, AL blocks TK6), **(b)** temperature fluctuations $T' := T - \bar{T}$ (24-h running mean subtracted) and gradient $\Delta T_{al}/\Delta z$, **(c)** AL airflow and wind speeds, and **(d)** measured AL heat fluxes. **(a, b)** AL air temperatures (TK1, —) and **(c)** AL airflow speeds down to 2.9 m (WS/1) show a daily course without time lag, only attenuated in amplitude. Rock temperatures (TK6, -··-) lag behind AL air temperatures. **(d)** Q_{HFP} HFP/1 is in phase with airflow speed and AL air temperature gradient, whereas Q_{CGR3}^{rad} is in phase with the lagging rock temperatures TK6/2.

The sensitivity of the apparent thermal diffusivity κ_a to a AL temperature gradients and its variability reflects how efficient convective heat transfer operates compared to radiation–conduction in the coarse-blocky AL. Wind-forced convection transfers some heat to large AL depths even under stable air stratification and increases the heat transfer rate compared to radiation–

conduction alone, at least in the comparatively large and highly permeable instrumented main cavity, otherwise κ_a would be a constant controlled only by the time-invariant debris properties (Fig. 10; excluding water phase changes). Sub-daily data show the mechanisms (Fig. 15): Driven by the anabatic atmospheric wind, AL airflow speeds are highest in the afternoon (Fig. 15b), precisely when the near-surface AL is most strongly heated and temperature gradient are largest (Fig. 15a). The (comparatively) strong afternoon winds counteract the stabilising positive temperature gradients. Warm air masses penetrate the permeable coarse-blocky AL. Forced convection transfers the heat downwards in the late morning–afternoon *parallel* (to recall the electrical analogue) to the radiative–conductive "background flux" (as shown by the TK1 and HFP/1 Q_{HFP} data; Fig. 15a, d), to which AL rock temperatures and the AL net long-wave radiation Q_{CGR3}^{rad} respond to with some time lag (TK6/2 and Q_{CGR3}^{rad} peak in the evening; Fig. 15a, d). This pattern of atmospheric wind speed, AL airflow speed, and AL air temperature gradients that co-vary in phase is in turn an effect of the low-albedo debris surface (micro-topography) in the sheltered cirque (macro-topography) that gives rise to insolation-driven diurnal cycles. Such daily oscillations of the AL air and rock temperatures without time lag down to $2.9\,\mathrm{m}$ that indicate non-conductive heat transfer were also observed by Herz (2006) in the *Ritigraben* block slope.

The important role of convection for the total heat transfer even at stable air stratification is plausible given the high intrinsic permeability $K\,[\mathrm{m}^2]$ of the Murtèl coarse-blocky AL in general and in particular at our measurement site, the instrumented cavity, and has been shown numerically by modelling studies (Pruessner et al., 2018; Wicky and Hauck, 2017, 2020). That implies, however, that the high values for κ_a or k_{eff} might be restricted to the ventilated near-surface AL and decrease with depth where (1) the intrinsic permeability is lower (more fine material), and (2) the influence of the atmosphere is weaker. Wicky and Hauck (2020) obtained a value of $K = 3 \times 10^{-6}\,\mathrm{m}^2$ as an effective landform average from numerical modelling. However, around the instrumented cavity, blocks/voids are comparatively large and the permeability likely even higher. The local Kozeny–Carman intrinsic permeability K_{KC} is estimated via (Wicky and Hauck, 2020)

$$K_{KC} = \frac{\phi_{al}^3}{5(6/d_{10})^2(1-\phi_{al})^2}, \tag{20}$$

which for a characteristic block diameter $d_{10} \approx 0.3\,\mathrm{m}$ yields $\sim 2 \times 10^{-5}\,\mathrm{m}^2$. This is a rough estimate from extrapolation, since the Kozeny–Carman relation has not been tested for such coarse material composed of non-spherical blocks and the airflow regime is far from Darcian (Wicky and Hauck, 2020; Côté et al., 2011).

6.2.2 Radiative heat transfer and stagnant effective thermal diffusivity κ_a^0

The effective thermal diffusivity under strongly stable air stratification (Fig. 10), where turbulence is suppressed and vertical airflow speed in the cavity is smallest (Fig. A2), is our best-available field estimate of the *stagnant* effective thermal diffusivity κ_a^0, i.e. $\sim$purely radiative–conductive with insignificant convection. A vertical temperature gradient of $4\,\mathrm{K\,m^{-1}}$ appears as the threshold above which the variation of κ_a is smaller (Fig. 10), which corresponds to $8\,°\mathrm{C}$ at mid-cavity level (ca. $2\,\mathrm{m}$ above the AL base at $0\,°\mathrm{C}$). Hanson and Hoelzle (2004) found the AL decoupled from the atmosphere above a threshold temperature of $6\,°\mathrm{C}$ (daily average temperature). Hence, our analysis is another view at their concept of 'non-linear heating

Table 5. Literature values for the apparent thermal diffusivity κ_a.

Value κ_a [m^2 s^{-1}]	Landform/context	Reference
2.3×10^{-6}	*Murtèl* rock glacier (ventilated)	this study
9.6×10^{-7}	*Murtèl* rock glacier (stagnant)	this study
$\sim 10^{-2}-10^{-5}$	*Murtèl–Chastelets* periglacial area	Hanson and Hoelzle (2005)
2.7×10^{-6}	*Chastelets* (AL)	Schneider et al. (2012)
$(1.3-1.6) \times 10^{-6}$	*Chastelets* (PF)	Schneider et al. (2012)
1.6×10^{-6}	*Murtèl* bedrock	Schneider et al. (2012)
$\sim 10^{-3}-10^{-4}$	*Ritigraben* block slope	Herz (2006)
2×10^{-7}	*Juvvasshøe* block field (AL)	Isaksen et al. (2003)
$(0.5-2.0) \times 10^{-5}$	openwork block field (stagnant)	Juliussen and Humlum (2008)
$\sim 7 \times 10^{-5}$	openwork block field (ventilated)	Juliussen and Humlum (2008)
$(6.0-9.0) \times 10^{-7}$	*Khumbu* debris covered glacier	Conway and Rasmussen (2000)
$(9.50 \pm 0.09) \times 10^{-7}$	debris-covered glacier	Nicholson and Benn (2013)
$(6.41 \pm 2.21) \times 10^{-7}$	*Lirung* debris-covered glacier	Steiner et al. (2021)
$(1.6-2.0) \times 10^{-7}$	cryic regosol	Mendoza López et al. (2023)

AL = active layer; PF = permafrost body. Rowan et al. (2021) tabulated k_{eff} for supraglacial debris.

of the AL with air temperature'. Also Herz (2006) interpreted that the *Ritigraben* block slope switches from a conduction- to convection-dominated regime at $4-6°$C.

Our estimate of the stagnant thermal conductivity $k_{\mathrm{eff}}^0 \approx 1.2$ W m^{-1} K^{-1}, derived from $\kappa_a^0 = 9.6 \times 10^{-7}$ m^2 s^{-1} via Eq. 15,
650   is $\sim 3\times$ higher than what would be expected from the geometric mean or empirical engineering parameterisations that ignore radiation, for example Johansen (1975)'s $k_{dry} = 0.039\phi^{-2.2} \pm 25\%$ for dry crushed rock (Côté and Konrad, 2005). This is despite a k_{eff}^0 uncertainty of $\sim 30\%$ given the uncertainties in κ.

Such a high value of k_{eff}^0 shows the importance of radiation as a heat transfer mechanism in coarse, open-work blocky material as pointed out by Johansen (1975), investigated by Scherler et al. (2014); Schneider (2014) for Murtèl, and experimentally
655   confirmed by Fillion et al. (2011) for crushed-rock beds (block sizes d_{10} values ranging from 92 to 150 mm). The crucial thing is that the radiative thermal conductivity increases with block/pore size (actually: the effective length for radiation between particles) and mean temperature cubed, $k_{\mathrm{eff}}^0 = k_r \sim (d_{10}, \; \sigma\bar{T}^3)$. The larger the pores and the distance between particles, the larger the surface temperature differences and the radiative thermal conductivity k_r since the resulting radiative flux

$$Q_r = E\sigma(T_2^4 - T_1^4) \tag{21}$$

660   is independent of the inter-particle distance (Fillion et al., 2011; Lebeau and Konrad, 2016). The radiative conductivity is obtained from linearisation of Eq. 21 to recast it as a flux–gradient relation (diffusion equation) of the form $Q_r := k_r (\Delta T/\Delta z)$

(using $(T_2^4 - T_1^4) \approx 4\bar{T}^3(T_2 - T_1)$, approximation valid for $(T_2 - T_1)/\bar{T} \ll 1$) (Rieksts et al., 2019),

$$k_r = 4Ed_{10}\sigma\bar{T}^3. \tag{22}$$

E is a (semi-empirical) exchange factor (that absorbs the surface emissivity ε and accounts for the particle arrangement), d_{10}
the effective particle diameter (10% of the whole material mass has particles smaller than d_{10}; Fillion et al. (2011)), σ the
Stefan-Boltzmann constant, and $\bar{T} := (T_1 + T_2)/2$ a characteristic mean temperature (Eq. 11 in Fillion et al. (2011)).

The contribution of non-conductive heat transfer both by radiation and air convection increases with block/pore size. We
emphasize that considerable variability in terms of dominant heat transfer mechanism and resulting k_{eff} can be expected
laterally over the rock glacier and with depth within the AL, where block/pore sizes and abundance of fine material vary.
Such a dominant role of air convection is specific to dry and highly permeable coarse blocky material (Wicky and Hauck,
2020; Johansen, 1975). The stagnant effective thermal conductivity scales as $k_{\text{eff}}^0 \propto d_{10}$ (Eq. 22), and the intrinsic permeability
as $K \propto d_{10}^2$ (Eq. 20; assuming sorted debris with little fine material where the effective d_{10} block diameter meaningfully
characterises the heat transfer processes). For example, using Fillion et al. (2011)'s Eq. 11, for $0.3 \le d_{10} \le 1.2$ m, yields
$1.15 \le k_{\text{eff}}^0 \le 3.5$ W m^{-1} K^{-1} ($\phi_{al} = 0.4$, $\varepsilon = 0.9$). The strong sensitivity of k_{eff} and K to debris texture already at a landform
scale needs be kept in mind when attempting to upscale from point-wise measurements. This is shown by the overall higher
κ_a values in a nearby cavity (TK5 in 'east cavity' at 1.3 m depth, Fig. A3). Finally, the (simplified) functional relation $k_r \sim$
$(d_{10}, \sigma\bar{T}^3)$ and Fillion et al. (2011)'s semi-empirical formula might become invalid for large blocks/voids ('particle non-
isothermality effect'; see Singh and Kaviany (1994); Ryan et al. (2020) that also provide a definition of "large").

6.3 Winter-time heat transfer

In winter (here defined by $T_{al} < 0°$C, frozen), the snow cover determines the winter-time ground thermal regime by controlling
the magnitude of the heat fluxes and the convective air exchange across the snow cover via *snow funnels*. This is shown by the
two contrasting winters 2020–2021 (average snow conditions, weak air circulation beneath a closed snow cover) and 2021–
2022 (snow-poor winter, strong air circulation beneath a semi-closed snow cover).

6.3.1 Heat transfer beneath a closed snow cover

In the moderately snow-rich winter 2020–2021, after closing of the snow cover in December, heat fluxes were small (< 2 W m^{-2})
and upwards (Fig. 7; 'closed snow cover' sensu Amschwand et al. (2023)). Heat transfer on a daily timescale appears diffusive
(case 1: $Q_{\text{CGR3}}^{rad} \propto Q_{\text{HFP}}$). The AL heat flux is not larger than the conductive heat flux Q_S across the snow cover as calculated
in Amschwand et al. (2023). The AL air column is near-isothermal (Fig. 6b, Table 3 ③) and weakly unstable (Fig. 6c ③;
subcritical Rayleigh numbers in Fig. 6a). The measurements of heat fluxes, airflow speed and temperature are close to their
instrumental accuracy.

6.3.2 Heat transfer beneath a semi-closed snow cover

In winter 2021–2022 with a semi-closed snow cover (sensu Amschwand et al. (2023)), we detected air circulation and large, rapid convective heat fluxes ($\leq 20-30$ W m^{-2}, case 2: $Q^{rad}_{\mathrm{CGR3}} \not\propto Q_{\mathrm{HFP}}$, Fig. 7). We see two air circulation patterns, both buoyancy-driven, that differ in terms of persistence in time, heat flux magnitude, vertical temperature profile, and Rayleigh numbers (local instability): *Rayleigh ventilation* (Marchenko, 2001; Millar et al., 2014) and *cold-air infiltration* (Herz, 2006). Their occurrence is controlled by the AL–atmosphere connectivity and the snow cover, not solely by the vertical temperature gradients.

Rayleigh ventilation events occur typically in autumn before the onset of a thick snow cover, for example in Oct 2020. With unimpeded AL–atmosphere exchange, it is an efficient ($20-30$ W m^{-2}, Fig. 7) top-down cooling mechanism associated with the characteristic negative AL temperature gradients (unstable air stratification, Fig. 6b Table 3 ④) and is diagnosed by supercritical Rayleigh numbers (Ra > Ra$_c$). Rayleigh ventilation events as a response to rapid atmospheric cooling are a short-lived, but efficient heat transfer mechanism. Thermal equilibrium is reached rapidly within hours–days, for example in Sep 2020 or 2022. It contributed to the sudden end of the 2022 thaw season, where the entire AL was cooled from 5 to 0°C within 1 day.

In contrast, during *cold-air infiltration* phases, the AL cools bottom-up slowly and persistently over longer periods (days–weeks) at moderate fluxes (≤ 10 W m^{-2}, Fig. 7). Cold-air infiltration shaped the ground thermal regime in Nov 2020 and throughout the snow-poor winter 2021–2022. It caused 5°C lower AL temperature minima compared to winter 2020–2021, although winter 2021–2022 was 0.4°C warmer (Nov-Mar average). Convective exchange with the atmosphere is shown by fluctuating AL temperatures and characteristic concave temperature profiles with a minimum at mid-cavity level ('bulges', Fig. 6b, Table 3 ③; (Herz et al., 2003b)) whose depth coincides with increased daily temperature amplitudes (Fig. 6c). Cooling at depth stabilizes the AL air column, shown as subcritical Rayleigh numbers (Ra < Ra$_c$), and leads to a net downward long-wave radiative transfer $Q^{rad}_{\mathrm{CGR3}} > 0$ like during the thaw season (although much smaller), opposite to the measured HFP/1 heat flux Q_{HFP} (Fig. 7). Modelling convective heat exchange with the Rayleigh number alone would miss this type of air circulation. The bottom-up cooling is accompanied by a bottom-up drying, since ventilation brings in 'fresh', dry outside air into the otherwise saturated AL (Fig. 16, Fig. 6d ③), opposite to the summertime evaporative top-down drying. In-phase diurnal oscillations of AL relative humidity, temperature differences between AL and surface temperatures ($T_s - \min\{T_{al}\}$), and strong nighttime ventilation recorded in the rock-glacier furrow (WS/6 in a topographic depression, Fig. A1) suggest that cold-air infiltration occurs in clear-sky nights. Radiatively cooled air on the snow surface, produced by the nocturnal negative radiation balance (Amschwand et al., 2023), infiltrates into the coarse-blocky AL (Herz, 2006). Cold-air infiltration is an effect of non-local static instability (Stull, 1991) that arise from interactions between AL and a permeable snow cover. The mechanics is analogous to the summertime nocturnal near-surface air circulation that switches on when the near-surface atmosphere cools below the near-surface AL (nocturnal Balch ventilation, Amschwand et al. (2023)).

The cold-air infiltration likely corresponds to the *cold-air drainage* described in the literature (Wakonigg, 1996; Delaloye and Lambiel, 2005; Millar et al., 2014) where the infiltrating cold air flows laterally downslope in the permeable AL beneath

725　the snow cover (convection–advection), analogous to the katabatic drainage flows above the snow cover (Amschwand et al., 2023). Cold-air drainage has been interpreted on Murtèl by Sutter (1996); Bernhard et al. (1998). Snow funnels were found to be aligned along furrows, and our WS/6 that showed the clearest nocturnal drainage signal is in fact located in a topographic depression where cold air is likely to converge. However, our isolated point-wise measurements could not reveal the lateral extent and connectivity of the air flow and we did not perform gas tracer tests (Popescu et al., 2017a). Here, we prefer the more

730　descriptive term 'infiltration' to 'drainage'.
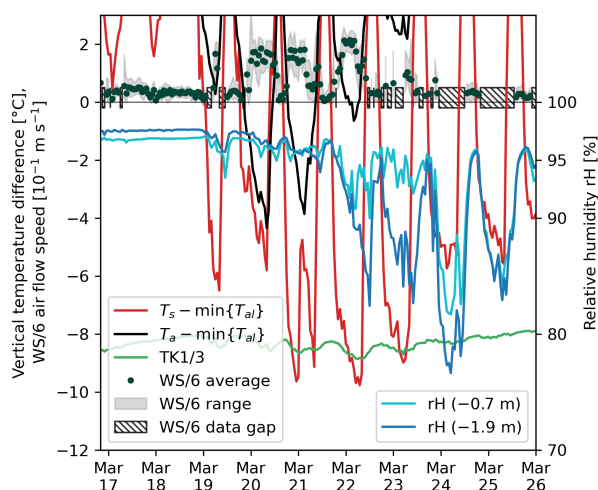
Figure 16. Nocturnal cold-air infiltration episodes in March 2022 as indicated by airflow speed measurement (WS/6) and a simultaneous drop of AL relative humidity (HV5/1–2) and temperature (TK1/3) due to the ventilation with fresh, dry-cold outside air. As soon as the ventilation stops, the AL air approaches saturation within hours. Higher WS/6 airflow speeds always coincide with negative $(T_s - \min\{T_{al}\})$. Using air temperature T_a instead of snow surface temperature T_s would underestimate the occurrence of cold-air infiltration episodes. Note the WS/6 data gaps due to power shortage.

7　Conclusions

We investigated heat transfer and storage processes in the ventilated coarse-blocky active layer (AL) of the seasonally snow-covered Murtèl rock glacier situated in a cirque in the Upper Engadine (eastern Swiss Alps). In the highly permeable AL, conductive/diffusive heat transfer including thermal radiation, non-conductive heat transfer by air circulation, and heat storage

735　changes from seasonal accretion and melting of ground ice shape the ground thermal regime. We provided estimates of subsurface heat flux and storage changes for the two-year period 2020–2022 based on a novel in-situ sensor array in the AL and direct observations of seasonal progression of the ground-ice table, i.e., ground ice melt. The measurements included thermistor strings, hygrometer, heat flux plates, and long-wave radiation sensors. Airflow speed sensors (thermo-anemometer) distributed in the AL revealed air circulation patterns. We parameterised the seasonal ground ice melt with a temperature index

740   model and a modified Stefan equation, whose key parameter, the effective thermal conductivity, was derived from the in-situ measurements.

The coarse-blocky AL intercepts the majority of the thaw-season ground heat flux of $\sim 5-15\ \mathrm{W\ m^{-2}}$ by melting ground ice ($\sim 70\%$; latent storage change that leaves the system as meltwater) and by heating the rock mass ($\sim 20\%$; sensible storage change). A smaller fraction ($\sim 10\%$) is transferred into the permafrost body beneath and causes slow permafrost degradation.

745   The cumulative heat uptake of $\sim 50-90\ \mathrm{MJ\ m^{-2}}$ during the thaw season is primarily controlled by the date of its onset, i.e. date of snow melt-out, and secondarily by the weather throughout the thaw season. Under radiation weather (high pressure, clear sky), daily-average AL temperature profiles were approximately linear. AL air temperature gradients were correlated with the measured daily-average sub-surface net long-wave radiation, suggesting that average air and rock temperatures converge: a local thermal equilibrium (LTE) is reached and diffusive heat flux (conduction in the blocks and thermal radiation in the pore

750   space) is dominant on a daily timescale when the AL air is stably stratified. A Stefan parametrisation based on steady-state heat conduction with field-measured bulk thermal conductivity and a temperature index model successfully simulated the seasonal ground ice melt.

Sub-daily measurements indicated convective heat transfer by *wind-forced convection* that enhances the diffusive (radiative–conductive) heat transfer in the highly permeable AL. This was reflected by time-varying thaw-season thermal diffusivity

755   κ_a values that decrease with increasing AL air temperature gradients from $2 \times 10^{-5}\ \mathrm{m^2\ s^{-1}}$ at labile air stratification to $\kappa_a^0 = 9.6 \times 10^{-7}\ \mathrm{m^2\ s^{-1}}$ at strongly stable air stratification. κ_a^0 corresponds to a stagnant, no-convection effective thermal conductivity $k_{\mathrm{eff}}^0 = 1.2\ \mathrm{W\ m^{-1}\ K^{-1}}$, which indicates that radiative heat exchange is an important heat transfer mechanism in coarse blocky material. This finding agrees with laboratory experiments with crushed-rock beds. Atmospheric wind tends to enhance mechanical turbulence in the AL and to increase κ_a. In snow-rich winters beneath a closed and insulating snow cover,

760   vertical heat fluxes are small (within $2\ \mathrm{W\ m^{-2}}$).

In contrast, in events of rapid atmospheric cooling that destabilises the AL air column (negative AL temperature gradients) and beneath a semi-closed snow cover in winter, buoyancy-driven convective heat transfer episodically prevails. In detail, we found two *buoyancy-driven convection* modes that differ in terms of their Rayleigh number, persistence in time, and associated heat fluxes. First, whenever the atmosphere cools faster than the AL, air density instabilities induce convective overturning

765   (*Rayleigh ventilation*), which is the most efficient cooling mechanism with episodic upward fluxes up to $\sim 20\ \mathrm{W\ m^{-2}}$. Second, at snow-free conditions or beneath a semi-closed early-winter snow cover perforated by snow funnels, radiatively cooled air infiltrates into the AL. *Cold-air infiltration*/drainage leads to moderate, but persistent fluxes of $\sim 2-5\ \mathrm{W\ m^{-2}}$ that result in strong convective winter cooling in snow-poor winters. This cooling mechanism is not diagnosed by Rayleigh numbers as the cold, dense air pools near the AL base, but should not be overlooked in future heat transfer modelling.

770   Such an important contribution of air convection to the total heat transfer is specific to highly permeable coarse blocky material. The two governing parameter, the bulk thermal conductivity k_{eff} (or the related apparent thermal diffusivity α_a) and the intrinsic permeability K are sensitive to debris texture. They might vary spatially with depth and laterally even on a landform scale. Furthermore, the contribution of buoyancy-driven convection to the total heat transfer varies temporally with the AL–atmosphere connectivity controlled by the snow cover and AL air stratification, hence k_{eff} is also sensitive to the

775 meteorological conditions. While this single-site case study provides important data and concepts towards the quantification of sub-surface heat fluxes in coarse-blocky landforms, more in-situ measurements other than ground temperatures together with laboratory experiments and numerical modelling are necessary for a comprehensive quantitative understanding.

Data availability. The PERMOS data can be obtained from the PERMOS network (http://www.permos.ch), and the PERMA-XT measurement data from https://www.permos.ch//doi/permos-spec-2023-1 (doi:10.13093/permos-spec-2023-01).

780 **Appendix A: Additional plots**
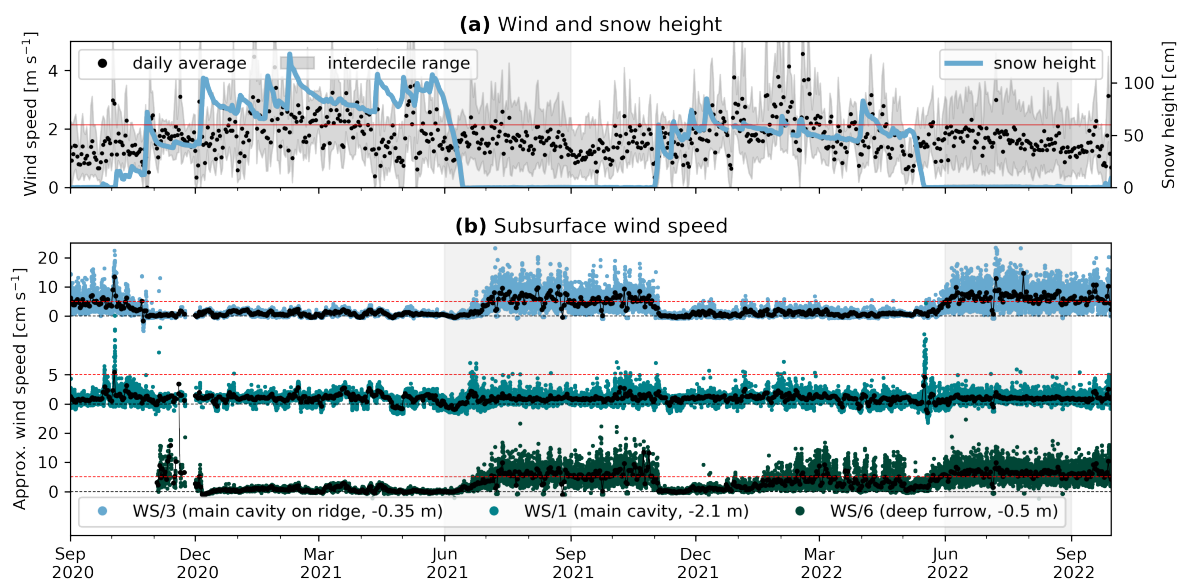
Figure A1. Sub-surface airflow speed (WS) measurements **(b)** with outside wind speed and snow for context **(a)**.
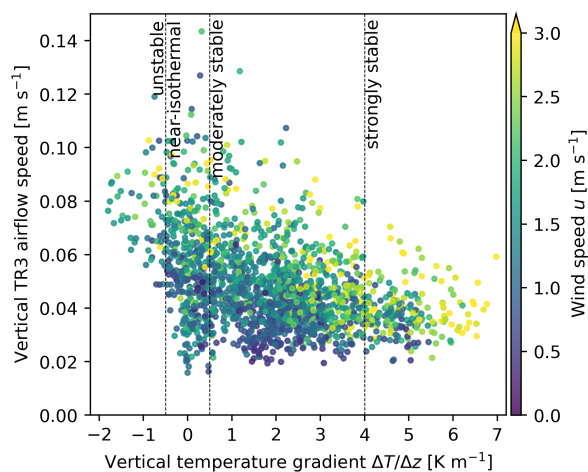
Figure A2. 3-h average vertical wind speed (TR3) tends to decrease with increasing temperature gradient (stable stratification suppresses airflow) and to increase with outside wind speed.

39
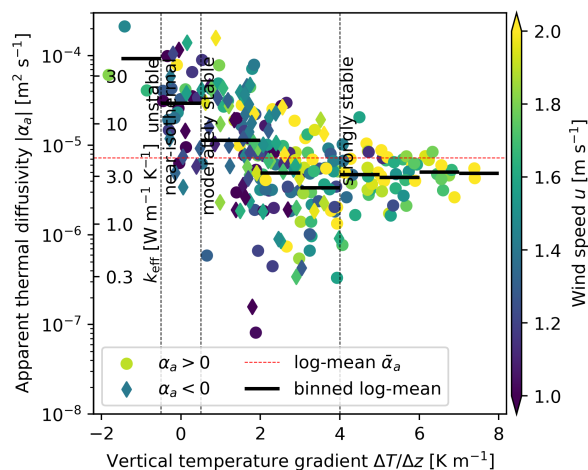
Figure A3. Apparent thermal diffusivity κ_a during the thaw seasons ($T_{al} > 1°\text{C}$) calculated from daily average AL temperatures in the east cavity (TK5; Eq. 17).

Author contributions. DA performed the fieldwork, model development and analyses for the study and wrote the manuscript. MS, MH and BK supervised the study, provided financial and field support and contributed to the manuscript preparation. AH and CK provided logistical support and editorial suggestions on the manuscript. HG designed the novel sensor array, regularly checked data quality, contributed to the analyses and provided editorial suggestions on the manuscript.

785   *Competing interests.* The authors declare that they have no conflict of interest.

790 **References**

Aldrich, H. P. and Paynter, H. M.: First Interim Report: Analytical Studies of Freezing and Thawing of Soils (ACFEL Technical Report No. 42), Tech. rep., US Corps of Engineers, Boston (MA), http://hdl.handle.net/11681/6526, Arctic Construction and Frost Effects Laboratory (ACFEL), 1953.

Amschwand, D., Scherler, M., Hoelzle, M., Krummenacher, B., Haberkorn, A., Kienholz, C., and Gubler, H.: Surface heat fluxes at coarse-
795   blocky Murtèl rock glacier (Engadine, eastern Swiss Alps), The Cryosphere Discussion, https://doi.org/10.5194/egusphere-2023-2109, 2023.

Arenson, L., Hoelzle, M., and Springman, S.: Borehole deformation measurements and internal structure of some rock glaciers in Switzerland, Permafrost and Periglacial Processes, 13, 117–135, https://doi.org/10.1002/ppp.414, 2002.

Arenson, L. U., Hauck, C., Hilbich, C., Seward, L., Yamamoto, Y., and Springman, S. M.: Sub-surface heterogeneities in the Murtèl-
800   Corvatsch rock glacier, Switzerland, in: Proceedings of the joint 63rd Canadian Geotechnical Conference and the 6th Canadian Permafrost Conference, pp. 1494–1500, Canadian Geotechnical Society, CNC-IPA/NRCan, Calgary, AB, Canada, 2010.

Bernhard, L., Sutter, F., Haeberli, W., and Keller, F.: Processes of snow/permafrost-interactions at a high mountain site, Murtèl/Corvatsch, eastern Swiss Alps, in: Proceedings of the 7th International Conference on Permafrost, 23–27 June 1998, Yellowknife, Northwest Territories, Canada, pp. 35–41, Centre d'Études Nordiques, Université Laval Saint-Foy (Québec), Canada, 1998.

805 Brighenti, S., Hotaling, S., Finn, D. S., Fountain, A. G., Hayashi, M., Herbst, D., Saros, J. E., Tronstad, L. M., and Millar, C. I.: Rock glaciers and related cold rocky landforms: Overlooked climate refugia for mountain biodiversity, Global Change Biology, 27, 1504–1517, https://doi.org/10.1111/gcb.15510, 2021.

Bächler, E.: Der verwünschte oder verhexte Wald im Brüeltobel, Appenzellerkalender, 209, https://doi.org/10.5169/seals-374836, 1930.

Conway, H. and Rasmussen, L. A.: Summer temperature profiles within supraglacial debris on Khumbu Glacier, Nepal, in: Debris-covered
810   Glaciers: Proceedings of an International Workshop Held at the University of Washington in Seattle, Washington, USA, 13-15 September 2000, edited by Fountain, A., Raymond, C. F., and Nakao, M., vol. 264 of *IAHS Proc. N. 264*, pp. 89–97, 2000.

Côté, J. and Konrad, J.-M.: Thermal conductivity of base-course materials, Canadian Geotechnical Journal, 42, 61–78, https://doi.org/10.1139/t04-081, 2005.

Côté, J., Fillion, M.-H., and Konrad, J.-M.: Intrinsic permeability of materials ranging from sand to rock-fill using natural air convection
815   tests, Canadian Geotechnical Journal, 48, 679–690, https://doi.org/10.1139/t10-097, 2011.

Delaloye, R. and Lambiel, C.: Evidence of winter ascending air circulation throughout talus slopes and rock glaciers situated in the lower belt of alpine discontinuous permafrost (Swiss Alps), Norsk Geografisk Tidsskrift – Norwegian Journal of Geography, 59, 194–203, https://doi.org/10.1080/00291950510020673, 2005.

Esence, T., Bruch, A., Molina, S., Stutz, B., and Fourmigué, J.-F.: A review on experience feedback and numerical modeling of packed-bed
820   thermal energy storage systems, Solar Energy, 153, 628–654, https://doi.org/10.1016/j.solener.2017.03.032, 2017.

Evatt, G. W., Abrahams, I. D., Heil, M., Mayer, C., Kingslake, J., Mitchell, S. L., Fowler, A. C., and Clark, C. D.: Glacial melt under a porous debris layer, Journal of Glaciology, 61, 825–836, https://doi.org/10.3189/2015JoG14J235, 2015.

Fillion, M.-H., Côté, J., and Konrad, J.-M.: Thermal radiation and conduction properties of materials ranging from sand to rock-fill, Canadian Geotechnical Journal, 48, 532–542, https://doi.org/10.1139/t10-093, 2011.

825 Frauenfelder, R. and Kääb, A.: Towards a palaeoclimatic model of rock-glacier formation in the Swiss Alps, Annals of Glaciology, 31, 281–286, https://doi.org/10.3189/172756400781820264, 2000.

Fujita, K. and Sakai, A.: Modelling runoff from a Himalayan debris-covered glacier, Hydrology and Earth System Sciences, 18, 2679–2694, https://doi.org/10.5194/hess-18-2679-2014, 2014.

Gorbunov, A. P., Marchenko, S. S., and Seversky, E. V.: The thermal environment of blocky materials in the mountains of Central Asia, Permafrost and Periglacial Processes, 15, 95–98, https://doi.org/10.1002/ppp.478, 2004.

Gruber, S. and Hoelzle, M.: The cooling effect of coarse blocks revisited: a modeling study of a purely conductive mechanism, in: Proceedings of the 9th International Conference on Permafrost, June 29–July 3 2008, Fairbanks, Alaska, edited by Kane, D. and Hinkel, K., pp. 557–561, Institute of Northern Engineering, University of Alaska, Fairbanks, Alaska, 2008.

Gubler, S., Fiddes, J., Keller, M., and Gruber, S.: Scale-dependent measurement and analysis of ground surface temperature variability in alpine terrain, The Cryosphere, 5, 431–443, https://doi.org/10.5194/tc-5-431-2011, 2011.

Guodong, C., Yuanming, L., Zhizhong, S., and Fan, J.: The 'thermal semi-conductor' effect of crushed rocks, Permafrost and Periglacial Processes, 18, 151–160, https://doi.org/10.1002/ppp.575, 2007.

Haeberli, W., Hallet, B., Arenson, L., Elconin, R., Humlum, O., Kääb, A., Kaufmann, V., Ladanyi, B., Matsuoka, N., Springman, S., and Mühll, D. V.: Permafrost creep and rock glacier dynamics, Permafrost and Periglacial Processes, 17, 189–214, https://doi.org/10.1002/ppp.561, 2006.

Hanson, S. and Hoelzle, M.: The thermal regime of the active layer at the Murtèl rock glacier based on data from 2002, Permafrost and Periglacial Processes, 15, 273–282, https://doi.org/10.1002/ppp.499, 2004.

Hanson, S. and Hoelzle, M.: Installation of a shallow borehole network and monitoring of the ground thermal regime of a high alpine discontinuous permafrost environment, Eastern Swiss Alps, Norsk Geografisk Tidsskrift – Norwegian Journal of Geography, 59, 84–93, https://doi.org/10.1080/00291950510020664, 2005.

Harris, S. A. and Pedersen, D. E.: Thermal regimes beneath coarse blocky materials, Permafrost and Periglacial Processes, 9, 107–120, https://doi.org/10.1002/(SICI)1099-1530(199804/06)9:2<107::AID-PPP277>3.0.CO;2-G, 1998.

Hayashi, M., Goeller, N., Quinton, W. L., and Wright, N.: A simple heat-conduction method for simulating the frost-table depth in hydrological models, Hydrological Processes, 21, 2610–2622, https://doi.org/10.1002/hyp.6792, 2007.

Herz, T.: Das Mikroklima grobblockiger Schutthalden der alpinen Periglazialstufe und seine Auswirkungen auf Energieaustauschprozesse zwischen Atmosphäre und Lithosphäre [The microclimate of coarse debris covers in the periglacial belt of high mountains and its effects on the energy exchange between atmosphere and lithosphere], PhD thesis, Justus-Liebig-Universität Gießen, 2006.

Herz, T., King, L., and Gubler, H.: Microclimate within coarse debris of talus slopes in the alpine periglacial belt and its effect on permafrost, in: Proceedings of the 8th International Conference on Permafrost, 21–25 July 2003, Zurich, Switzerland, edited by Phillips, M., Springman, S. M., and Arenson, L. U., pp. 383–387, Swets & Zeitlinger, Lisse, Zürich, 2003a.

Herz, T., King, L., and Gubler, H.: Thermal regime of coarse debris layers in the Ritigraben catchment, Matter Valley, Swiss Alps, in: Extended abstracts of the 8th International Conference on Permafrost, 21–25 July 2003, Zurich, Switzerland, edited by Haeberli, W. and Brandová, D., pp. 61–62, Swets & Zeitlinger, Lisse, Zürich, 2003b.

Hinkel, K. M., Outcalt, S. I., and Nelson, F. E.: Temperature variation and apparent thermal diffusivity in the refreezing active layer, Toolik Lake, Alaska, Permafrost and Periglacial Processes, 1, 265–274, https://doi.org/10.1002/ppp.3430010306, 1990.

Hock, R.: Temperature index melt modelling in mountain areas, Journal of Hydrology, 282, 104–115, https://doi.org/10.1016/S0022-1694(03)00257-9, 2003.

Hoelzle, M. and Gruber, S.: Borehole and ground surface temperatures and their relationship to meteorological conditions in the Swiss Alps, in: Proceedings of the 9th International Conference on Permafrost, June 29–July 3 2008, Fairbanks, Alaska, edited by Kane, D.

865   and Hinkel, K., pp. 723–728, Institute of Northern Engineering, University of Alaska, Fairbanks, Alaska, ISBN 978-0-9800179-2-2, https://doi.org/10.5167/uzh-2825, 2008.

Hoelzle, M., Wegmann, M., and Krummenacher, B.: Miniature temperature dataloggers for mapping and monitoring of permafrost in high mountain areas: first experience from the Swiss Alps, Permafrost and Periglacial Processes, 10, 113–124, https://doi.org/10.1002/(SICI)1099-1530(199904/06)10:2<113::AID-PPP317>3.0.CO;2-A, 1999.

870   Hoelzle, M., Mittaz, C., Etzelmüller, B., and Haeberli, W.: Surface energy fluxes and distribution models of permafrost in European mountain areas: an overview of current developments, Permafrost and Periglacial Processes, 12, 53–68, https://doi.org/10.1002/ppp.385, 2001.

Hoelzle, M., Mühll, D. V., and Haeberli, W.: Thirty years of permafrost research in the Corvatsch–Furtschellas area, Eastern Swiss Alps: A review, Norsk Geografisk Tidsskrift – Norwegian Journal of Geography, 56, 137–145, https://doi.org/10.1080/002919502760056468, 2002.

875   Hoelzle, M., Haeberli, W., and Stocker-Mittaz, C.: Miniature ground temperature data logger measurements 2000–2002 in the Murtèl-Corvatsch area, Eastern Swiss Alps, in: Proceedings of the 8th International Conference on Permafrost, 21–25 July 2003, Zurich, Switzerland, edited by Phillips, M., Springman, S. M., and Arenson, L. U., pp. 419–424, Swets & Zeitlinger, Lisse, Zürich, 2003.

Hoelzle, M., Hauck, C., Mathys, T., Noetzli, J., Pellet, C., and Scherler, M.: Long-term energy balance measurements at three different mountain permafrost sites in the Swiss Alps, Earth System Science Data, 14, 1531–1547, https://doi.org/10.5194/essd-14-1531-2022, 880   2022.

Hukseflux HFP manual: Manual for the Hukseflux HFP01 & HFP03 sensors heat flux plate / heat flux sensor (HFP manual v1721), Tech. rep., Delft: Hukseflux Thermal Sensors, 2016.

Hukseflux WS01 manual: Manual for the Hukseflux WS01 sensor for ultra low wind speeds and boundary layer conductance (WS01 manual v0608), Tech. rep., Delft: Hukseflux Thermal Sensors, 2006.

885   Humlum, O.: Active layer thermal regime at three rock glaciers in Greenland, Permafrost and Periglacial Processes, 8, 383–408, https://doi.org/10.1002/(SICI)1099-1530(199710/12)8:4<383::AID-PPP265>3.0.CO;2-V, 1997.

Isaksen, K., Heggem, E., Bakkehøi, S., Ødegård, R., Eiken, T., Etzelmüller, B., and Sollid, J.: Mountain permafrost and energy balance on Juvvasshøe, southern Norway, in: Proceedings of the 8th International Conference on Permafrost, 21–25 July 2003, Zurich, Switzerland, edited by Phillips, M., Springman, S., and Arenson, L., pp. 467–472, Swets & Zeitlinger, Lisse, Zürich, 2003.

890   Johansen, Ø.: Thermal conductivity of soils (CRREL Draft Translation 637, 1977), Tech. rep., 1975.

Juliussen, H. and Humlum, O.: Thermal regime of openwork block fields on the mountains Elgåhogna and Sølen, central-eastern Norway, Permafrost and Periglacial Processes, 19, 1–18, https://doi.org/10.1002/ppp.607, 2008.

Kääb, A., Gudmundsson, G. H., and Hoelzle, M.: Surface deformation of creeping mountain permafrost. Photogrammetric investigations on Murtèl rock glacier, Swiss Alps, in: Proceedings of the 7th International Conference on Permafrost, 23–27 June 1998, Yellowknife, 895   Northwest Territories, Canada, pp. 531–537, Université Laval, 1998.

Kane, D. L., Hinkel, K. M., Goering, D. J., Hinzman, L. D., and Outcalt, S. I.: Non-conductive heat transfer associated with frozen soils, Global and Planetary Change, 29, 275–292, https://doi.org/10.1016/S0921-8181(01)00095-9, 2001.

Kayastha, R. B., Takeuchi, Y., Nakawo, M., and Ageta, Y.: Practical prediction of ice melting beneath various thickness of debris cover on Khumbu Glacier, Nepal, using a positive degree-day factor, in: Debris-covered Glaciers: Proceedings of an International Workshop Held 900   at the University of Washington in Seattle, Washington, USA, 13-15 September 2000, edited by Fountain, A., Raymond, C. F., and Nakao, M., vol. 264 of *IAHS Proc. N. 264*, pp. 71–81, 2000.

Keller, F. and Gubler, H.: Interaction between snow cover and high mountain permafrost: Murtèl/Corvatsch, Swiss Alps, in: Proceedings of the 6th International Conference on Permafrost, July 5–9 1993, Beijing, China, edited by Guodong, C., vol. 1, pp. 332–337, Lanzhou Institute of Glaciology and Geocryology, Chinese Academy of Sciences & Chinese Society of Glaciology and Geocryology, South China University of Technology Press, 1993.

Kipp & Zonen CGR3 manual: Manual for the Kipp & Zonen CGR 4 pyrgeometer (v1401), Tech. rep., Delft: Kipp & Zonen, 2014.

Kneisel, C., Hauck, C., and Vonder Mühll, D.: Permafrost below the Timberline Confirmed and Characterized by Geoelectrical Resistivity Measurements, Bever Valley, Eastern Swiss Alps, Permafrost and Periglacial Processes, 11, 295–304, https://doi.org/10.1002/1099-1530(200012)11:4<295::AID-PPP353>3.0.CO;2-L, 2000.

Kurylyk, B. L.: Discussion of 'A simple thaw-freeze algorithm for a multi-layered soil using the Stefan equation' by Xie and Gough (2013), Permafrost and Periglacial Processes, 26, 200–206, https://doi.org/10.1002/ppp.1834, 2015.

Kurylyk, B. L. and Hayashi, M.: Improved Stefan equation correction factors to accommodate sensible heat storage during soil freezing or thawing, Permafrost and Periglacial Processes, 27, 189–203, https://doi.org/10.1002/ppp.1865, 2016.

Lebeau, M. and Konrad, J.-M.: Non-Darcy flow and thermal radiation in convective embankment modeling, Computers and Geotechnics, 73, 91–99, https://doi.org/10.1016/j.compgeo.2015.11.016, 2016.

Luetschg, M., Lehning, M., and Haeberli, W.: A sensitivity study of factors influencing warm/thin permafrost in the Swiss Alps, Journal of Glaciology, 54, 696–704, https://doi.org/10.3189/002214308786570881, 2008.

Marchenko, S. S.: A model of permafrost formation and occurrences in the intracontinental mountains, Norsk Geografisk Tidsskrift – Norwegian Journal of Geography, 55, 230–234, https://doi.org/10.1080/00291950152746577, 2001.

Mellor, M.: Engineering Properties of Snow, Journal of Glaciology, 19, 15–66, https://doi.org/10.3189/S002214300002921X, 1977.

Mendoza López, M., Tapia Baldis, C., Trombotto Liaudat, D., and Sileo, N.: Thermal simulations on periglacial soils of the Central Andes, Argentina, Permafrost and Periglacial Processes, n/a, https://doi.org/10.1002/ppp.2189, 2023.

Mihalcea, C., Mayer, C., Diolaiuti, G., Lambrecht, A., Smiraglia, C., and Tartari, G.: Ice ablation and meteorological conditions on the debris-covered area of Baltoro glacier, Karakoram, Pakistan, Annals of Glaciology, 43, 292–300, https://doi.org/10.3189/172756406781812104, 2006.

Millar, C. I., Westfall, R. D., and Delany, D. L.: Thermal regimes and snowpack relations of periglacial talus slopes, Sierra Nevada, California, U.S.A., Arctic, Antarctic, and Alpine Research, 46, 483–504, https://doi.org/10.1657/1938-4246-46.2.483, 2014.

Mittaz, C., Hoelzle, M., and Haeberli, W.: First results and interpretation of energy-flux measurements over Alpine permafrost, Annals of Glaciology, 31, 275–280, https://doi.org/10.3189/172756400781820363, 2000.

Mollaret, C., Wagner, F. M., Hilbich, C., Scapozza, C., and Hauck, C.: Petrophysical Joint Inversion Applied to Alpine Permafrost Field Sites to Image Subsurface Ice, Water, Air, and Rock Contents, Frontiers in Earth Science, 8, https://doi.org/10.3389/feart.2020.00085, 2020.

Naguel, C.: Permafrostvorkommen in der Frontpartie und räumliche und zeitliche Repräsentativität von BTS-Messungen: Untersuchungen an zwei Blockgletschem im Oberengadin, Master's thesis, Geographisches Institut der Universität Zürich, 1998.

Nakawo, M. and Young, G.: Field Experiments to Determine the Effect of a Debris Layer on Ablation of Glacier Ice, Annals of Glaciology, 2, 85–91, https://doi.org/10.3189/172756481794352432, 1981.

Nakawo, M. and Young, G.: Estimate of Glacier Ablation under a Debris Layer from Surface Temperature and Meteorological Variables, Journal of Glaciology, 28, 29–34, https://doi.org/10.3189/S002214300001176X, 1982.

Nicholson, L. and Benn, D. I.: Calculating ice melt beneath a debris layer using meteorological data, Journal of Glaciology, 52, 463–470, https://doi.org/10.3189/172756506781828584, 2006.

940 Nicholson, L. and Benn, D. I.: Properties of natural supraglacial debris in relation to modelling sub-debris ice ablation, Earth Surface Processes and Landforms, 38, 490–501, https://doi.org/10.1002/esp.3299, 2013.

Nield, D. A. and Bejan, A.: Convection in Porous Media, Springer, New York, 5 edn., https://doi.org/10.1007/978-3-319-49562-0, 2017.

Nixon, J. F. and McRoberts, E. C.: A Study of Some Factors Affecting the Thawing of Frozen Soils, Canadian Geotechnical Journal, 10, 439–452, https://doi.org/10.1139/t73-037, 1973.

945 Noetzli, J., Pellet, C., and Staub, B., eds.: Permafrost in Switzerland 2014/2015 to 2017/2018, Glaciological Report Permafrost No. 16–19 (PERMOS Report 2019), Fribourg: Cryospheric Commission of the Swiss Academy of Sciences, https://doi.org/10.13093/permos-rep-2019-16-19, 2019.

Oswald, M.: Luftzirkulation in der Auftauschicht des Blockgletschers Chastelets, Master's thesis, Geographisches Institut der Universität Zürich, 2004.

950 Panz, M.: Analyse von Austauschprozessen in der Auftauschicht des Blockgletschers Murtèl, Corvatsch, Oberengadin, Master's thesis, Geographisches Institut der Ruhr-Universität Bochum, 2008.

Petersen, E., Hock, R., Fochesatto, G. J., and Anderson, L. S.: The significance of convection in supraglacial debris revealed through novel analysis of thermistor profiles, Journal of Geophysical Research: Earth Surface, 127, e2021JF006 520, https://doi.org/10.1029/2021JF006520, 2022.

955 Popescu, R., Onaca, A., Urdea, P., and Vespremeanu-Stroe, A.: Landform Dynamics and Evolution in Romania, chap. Spatial Distribution and Main Characteristics of Alpine Permafrost from Southern Carpathians, Romania, pp. 117–146, Springer International Publishing, Cham, ISBN 978-3-319-32589-7, https://doi.org/10.1007/978-3-319-32589-7_6, 2017a.

Popescu, R., Vespremeanu-Stroe, A., Onaca, A., Vasile, M., Cruceru, N., and Pop, O.: Low-altitude permafrost research in an overcooled talus slope–rock glacier system in the Romanian Carpathians (Detunata Goală, Apuseni Mountains), Geomorphology, 295, 840–854,
960 https://doi.org/10.1016/j.geomorph.2017.07.029, 2017b.

Pruessner, L., Phillips, M., Farinotti, D., Hoelzle, M., and Lehning, M.: Near-surface ventilation as a key for modeling the thermal regime of coarse blocky rock glaciers, Permafrost and Periglacial Processes, 29, 152–163, https://doi.org/10.1002/ppp.1978, 2018.

Rana, B., Nakawo, M., Fukushima, Y., and Agkta, Y.: Application of a conceptual precipitation-runoff model (HYGY-MODEL) in a debris-covered glacierized basin in the Langtang Valley, Nepal Himalaya, Annals of Glaciology, 25, 226–231,
965 https://doi.org/10.3189/S0260305500014087, 1997.

Renette, C., Aalstad, K., Aga, J., Zweigel, R. B., Etzelmüller, B., Lilleøren, K. S., Isaksen, K., and Westermann, S.: Simulating the effect of subsurface drainage on the thermal regime and ground ice in blocky terrain in Norway, Earth Surface Dynamics, 11, 33–50, https://doi.org/10.5194/esurf-11-33-2023, 2023.

Rieksts, K., Hoff, I., Scibilia, E., and Côté, J.: Laboratory investigations into convective heat transfer in road construction materials, Canadian
970 Geotechnical Journal, 57, 959–973, https://doi.org/10.1139/cgj-2018-0530, 2019.

Rist, A.: Hydrothermal processes within the active layer above alpine permafrost in steep scree slopes and their influence on slope stability, PhD thesis, University of Zurich, Zürich, https://doi.org/10.5167/uzh-163579, 2007.

Rist, A. and Phillips, M.: First results of investigations on hydrothermal processes within the active layer above alpine permafrost in steep terrain, Norsk Geografisk Tidsskrift – Norwegian Journal of Geography, 59, 177–183, https://doi.org/10.1080/00291950510020574, 2005.

975 Rist, A., Phillips, M., and Auerswald, K.: Undercooled scree slopes covered with stunted dwarf trees in Switzerland – abiotic factors to characterize the phenomenon, in: Extended Abstracts of the 8th International Conference on Permafrost, 21–25 July 2003, Zurich, Switzerland, edited by Haeberli, W. and Brandovà, D., pp. 135–136, 2003.

Roth, K. and Boike, J.: Quantifying the thermal dynamics of a permafrost site near Ny-Ålesund, Svalbard, Water Resources Research, 37, 2901–2914, https://doi.org/10.1029/2000WR000163, 2001.

980   Rounce, D. R. and McKinney, D. C.: Debris thickness of glaciers in the Everest area (Nepal Himalaya) derived from satellite imagery using a nonlinear energy balance model, The Cryosphere, 8, 1317–1329, https://doi.org/10.5194/tc-8-1317-2014, 2014.

Rowan, A. V., Nicholson, L. I., Quincey, D. J., Gibson, M. J., Irvine-Fynn, T. D., Watson, C. S., Wagnon, P., Rounce, D. R., Thompson, S. S., Porter, P. R., and et al.: Seasonally stable temperature gradients through supraglacial debris in the Everest region of Nepal, Central Himalaya, Journal of Glaciology, 67, 170–181, https://doi.org/10.1017/jog.2020.100, 2021.

985   Ryan, A. J., Pino Muñoz, D., Bernacki, M., and Delbo, M.: Full-Field Modeling of Heat Transfer in Asteroid Regolith: 1. Radiative Thermal Conductivity of Polydisperse Particulates, Journal of Geophysical Research: Planets, 125, https://doi.org/10.1029/2019JE006100, 2020.

Sakai, A., Fujita, K., and Kubota, J.: Evaporation and percolation effect on melting at debris-covered Lirung Glacier, Nepal Himalayas, 1996, Bulletin of Glaciological Research, 21, 9–15, 2004.

Sawada, Y.: Monitoring of ground-ice formation in a block slope at Mt. Nishi-Nupukaushinupuri, Hokkaido, Japan, in: Proceedings of the

990   8th International Conference on Permafrost, 21–25 July 2003, Zurich, Switzerland, edited by Phillips, M., Springman, S. M., and Arenson, L. U., pp. 1001–1005, Swets & Zeitlinger, Lisse, Zürich, 2003.

Sawada, Y., Ishikawa, M., and Ono, Y.: Thermal regime of sporadic permafrost in a block slope on Mt. Nishi-Nupukaushinupuri, Hokkaido Island, Northern Japan, Geomorphology, 52, 121–130, https://doi.org/10.1016/S0169-555X(02)00252-0, 2003.

Scherler, M., Schneider, S., Hoelzle, M., and Hauck, C.: A two-sided approach to estimate heat transfer processes within the active layer of

995   the Murtèl–Corvatsch rock glacier, Earth Surface Dynamics, 2, 141–154, https://doi.org/10.5194/esurf-2-141-2014, 2014.

Schneider, S.: The heterogeneity of mountain permafrost – A field-based analysis of different periglacial materials, PhD thesis, University of Fribourg (Switzerland), 2014.

Schneider, S., Hoelzle, M., and Hauck, C.: Influence of surface and subsurface heterogeneity on observed borehole temperatures at a mountain permafrost site in the Upper Engadine, Swiss Alps, The Cryosphere, 6, 517–531, https://doi.org/10.5194/tc-6-517-2012, 2012.

1000   Schneider, S., Daengeli, S., Hauck, C., and Hoelzle, M.: A spatial and temporal analysis of different periglacial materials by using geo-electrical, seismic and borehole temperature data at Murtèl–Corvatsch, Upper Engadin, Swiss Alps, Geographica Helvetica, 68, 265–280, https://doi.org/10.5194/gh-68-265-2013, 2013.

Schuepp, P. H.: Tansley review No. 59. Leaf boundary layers, New Phytologist, pp. 477–507, 1993.

Singh, B. and Kaviany, M.: Effect of solid conductivity on radiative heat transfer in packed beds, International Journal of Heat and Mass

1005   Transfer, 37, 2579–2583, https://doi.org/10.1016/0017-9310(94)90295-x, 1994.

Staub, B., Hasler, A., Noetzli, J., and Delaloye, R.: Gap-filling algorithm for ground surface temperature data measured in permafrost and periglacial environments, Permafrost and Periglacial Processes, 28, 275–285, https://doi.org/10.1002/ppp.1913, 2017.

Steiner, J. F., Kraaijenbrink, P. D. A., and Immerzeel, W. W.: Distributed melt on a debris-covered glacier: Field observations and melt modeling on the Lirung Glacier in the Himalaya, Frontiers in Earth Science, 9, 567, https://doi.org/10.3389/feart.2021.678375, 2021.

1010   Stocker-Mittaz, C., Hoelzle, M., and Haeberli, W.: Modelling alpine permafrost distribution based on energy-balance data: a first step, Permafrost and Periglacial Processes, 13, 271–282, https://doi.org/10.1002/ppp.426, 2002.

Stull, R. B.: Static stability–an update, Bulletin of the American Meteorological Society, 72, 1521–1529, https://doi.org/10.1175/1520-0477(1991)072<1521:SSU>2.0.CO;2, 1991.

Sutter, F.: Untersuchung von Schloten in der Schneedecke des Blockgletschers Murtel am Corvatsch, Master's thesis, Geographisches Institut

1015   der Universität Zürich, 1996.

Tenthorey, G. and Gerber, E.: Hydrologie du glacier rocheux de Murtèl (Grisons). Description et interprétation de traçages d'eau, in: Modèles en Géomorphologie – exemples Suisses. Session scientfique de la Société suisse de Géomorphologie. Fribourg, 22/23 juin 1990., edited by Monbaron, M. and Haeberli, W., vol. 3 of *Rapport et recherches, Institut de Géographie Fribourg*, 1991.

TriSonica Mini sensor manual: Manual for the Anemoment TriSonica mini wind & weather sensor, Tech. rep., Longmont (CO): Anemoment LLC, 2021.

Vonder Mühll, D. and Haeberli, W.: Thermal characteristics of the permafrost within an active rock glacier (Murtèl/Corvatsch, Grisons, Swiss Alps), Journal of Glaciology, 36, 151–158, https://doi.org/10.3189/S0022143000009382, 1990.

Vonder Mühll, D. S.: Drilling in Alpine permafrost, Norsk Geografisk Tidsskrift – Norwegian Journal of Geography, 50, 17–24, https://doi.org/10.1080/00291959608552348, 1996.

Wakonigg, H.: Unterkühlte Schutthalden [Undercooled talus], Arbeiten aus dem Institut für Geographie der Karl-Franzens Universität Graz, 33, 209–223, 1996.

Wicky, J. and Hauck, C.: Numerical modelling of convective heat transport by air flow in permafrost talus slopes, The Cryosphere, 11, 1311–1325, https://doi.org/10.5194/tc-11-1311-2017, 2017.

Wicky, J. and Hauck, C.: Air convection in the active layer of rock glaciers, Frontiers in Earth Science, 8, 335, https://doi.org/10.3389/feart.2020.00335, 2020.

Woo, M.-k. and Xia, Z.: Effects of Hydrology on the Thermal Conditions of the Active Layer: Paper presented at the 10th Northern Res. Basin Symposium (Svalbard, Norway — 28 Aug./3 Sept. 1994), Hydrology Research, 27, 129–142, https://doi.org/10.2166/nh.1996.0024, 1996.

Yoshikawa, K., Schorghofer, N., and Klasner, F.: Permafrost and seasonal frost thermal dynamics over fifty years on tropical Maunakea volcano, Hawai'i, Arctic, Antarctic, and Alpine Research, 55, 2186 485, https://doi.org/10.1080/15230430.2023.2186485, 2023.

Zhang, T.: Influence of the seasonal snow cover on the ground thermal regime: An overview, Reviews of Geophysics, 43, https://doi.org/10.1029/2004RG000157, 2005.